Redistribution of sidechain-sidechain interactions govern ligand-specific binding affinity changes in missense Shank1 PDZ mutants

1 Authors

Anna Sánta[1], Zsófia E. Kálmán[1], Eszter Nagy-Kanta[1], Zoltán Gáspári[1], Bálint Péterfia[1*]

[1]Faculty of Information Technology and Bionics, Pázmány Péter Catholic University, Budapest, Hungary

*corresponding author

2 Abstract

Shank proteins represent a family of abundant scaffolds in the postsynaptic density. Their dysfunctions had been identified as possible causes behind autism spectrum disorders and various types of cancer. The remarkably promiscuous PDZ domain of the Shank family is highly conserved through isoforms, and contains a unique dynamic segment, the β2-β3 loop, which is likely to play an important role in ligand selectivity. We used the Shank1 PDZ as a model system to analyze the perturbing effects of five disease-associated missense mutations on the binding of different partner peptides. Using experimental methods and molecular dynamics simulations, we characterized the interactions in detail, focusing on their dynamic aspect. While the investigated mutations in general weaken most interactions, the R736Q mutant, unique in having increased thermal stability, also binds the GKAP peptide with higher affinity than the wild type. Overall, our results show that the perturbing effect of mutations is highly partner-specific and depends on the dynamic rearrangements of both uniformly occurring and ligand-specific residue-residue interactions.

Keywords (7): Postsynaptic density; PDZ domain; peptide binding; dynamics; missense mutation; MD simulation

3 Introduction

Shank1, member of the Shank family consisting of three proteins, is one of the major scaffolding proteins at the postsynaptic density (PSD) of excitatory synapses composed of ankyrin-repeat-, SH3-, PDZ- and SAM domains as well as a long, proline-rich disordered region. [1] ***(Fig. 1A)*** Due to these protein interacting domains and regions, Shank1 is able to form supramolecular complexes with a great number of other proteins. Shank1 has been associated with neurological disorders such as autism spectrum disorder, schizophrenia, mental disability and recently, its role in tumor progression has also been revealed. The PDZ domain of Shank1 is a remarkably promiscuous Class I PDZ domain, with a unique b1-b2 loop region that is only found in the Shank family. Otherwise, its secondary structure composition is highly conserved, as well as its regions involved in partner binding. Structural features of its bound state are well documented via experimentally determined structures, with several binding partners, especially GKAP. [2–7] ***(Fig. 1B, 1C, 1D)***

Regarding neural disorders, unlike Shank2 or -3, Shank1 is known to be expressed predominantly in the brain, in a distinctly different pattern with highest abundance in the cortex, cerebellum and hippocampus. Shank1 knockout mice exhibit a complex behavioral phenotype and decreased expression of GKAP and Homer proteins, which are well-known direct interaction partners of Shank1. The C terminus of GKAP is bound to the PDZ domain

of Shank1, while Homer interacts with the Proline-rich segment. So far, Shank1 have been regarded as a low risk ASD gene probably due to the obscure, mild phenotype of KO mice - unlike Shank3, which is associated with severe autism-like symptoms in KO mouse models, and is the cause of Phelan-McDermid syndrome in humans. Lack of Shank3 results in downregulation of the Akt/mTORC1 pathway, resulting in decreased protein synthesis and neuronal dysfunction. [8] However, recently, knock-in mice bearing the R882H missense mutation (localized downstream to the PDZ domain) have been reported to display core ASD symptoms with social disability and repetitive behaviors due to downregulation of mGluR1-Homer-IP3R1-calcium signaling. [9] This finding underlines that missense mutations are promising tools to explore the role that Shank proteins and their domains play in neural disorders. This suggests that loss-of PDZ domain missense mutations could be used to elucidate the role of the GKAP-Shank1 interaction (and other PDZ interactions) in neurological disorders. Only one missense mutation of the Shank1 PDZ domain (R736Q) is described in relation to ASD, but its pathogenicity is uncertain. [10]

Beyond their synaptic functions, Shank proteins have been recognized to play a role in several malignancies with altered expression and survival correlation. [11–13] Shank expression or DNA methylation are independent prognostic markers in colon cancer and leukemia. [14,15] In addition, the expression of Shank proteins regulates the fate and development of stem cells through different signaling pathways. [16] Shank1 has been studied in non-small cell lung and colon cancer. [17] The tumor promoting effects of Shank1 were found to be mediated by the AKT/mTOR signaling pathway in colon cancer cell lines, and by MDM2 in NSCLC cells. [14,17] Nuclear translocation of MDM2 is known to be triggered by the AKT/mTOR pathway, which suggests a common pathway of Shank1 in these cell lines. There is no direct evidence as to which domain of Shank1 may play a role in activating the Akt/mTOR pathway.

Deletion of the PDZ domain causes Shank2 to lose its oncogenicity via Hippo signaling, but whether Shank1 or Shank3 also participate in this pathway is unknown. The aforementioned Shank2 pathway is driven by the interaction with ARHGEF7 (βPIX), also a known interaction partner of the Shank1 PDZ. [11]

As of now, no mouse model is known that was created with the aim of modeling oncogenic behavior of Shank1 specifically. Xenograft experiments with overexpressed Shank1 and Shank2 showed tumor promoting effects. [11,17] No specific point mutations of Shank1 are known to be directly associated with cancer. However, several point mutations found in tumor samples are documented in the COSMIC database. [18] ***(Fig. 1E)***

To avoid investing significant effort in generating transgenic mice with neutral benign point mutations, it is crucial to experimentally characterize potential variants in vitro. This study examines the effects of one ASD-associated and four somatic missense variants of the Shank1 PDZ domain on partner binding capacity and structure in vitro, starting with GKAP as the reference model, and expanding to four other partners with possible clinical significance. From these additional partners, βPIX bears a C-terminal binding motif, whereas ARAP3, ATG13 and mTOR exhibit internal binding sequences. We assess the thermal stability and binding properties of the Shank1 PDZ mutants and use molecular dynamics simulations to aid the interpretation of our findings.

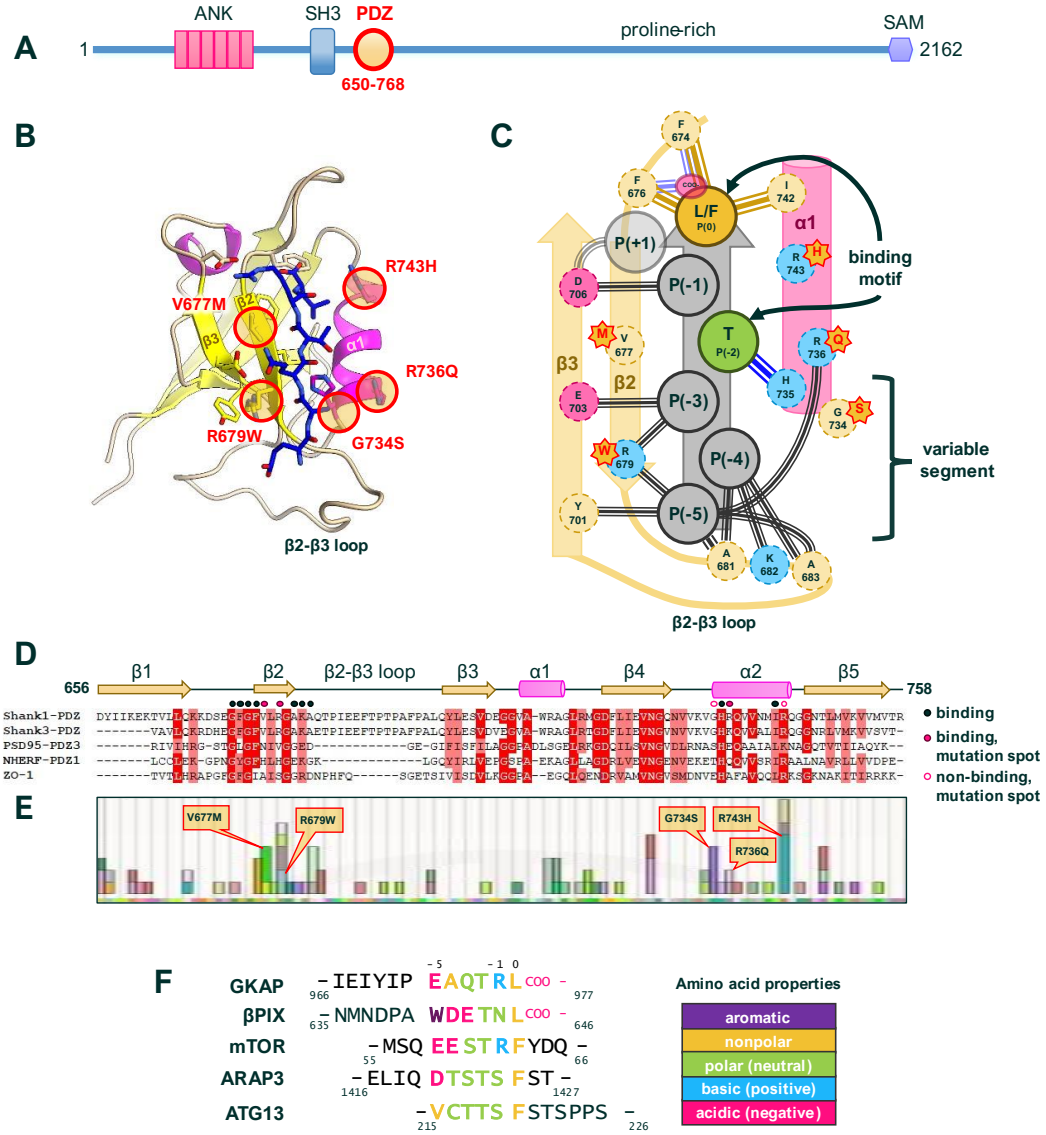

Figure 1. The Shank1 PDZ and its binding modes. (A) Domain composition of the Shank1 protein, with the PDZ domain and the span of our construct highlighted in red (the canonical PDZ spans from 663-757). For a list of constructs, refer to the Supplementary Tables. **(B)** Structure model of the Shank1 PDZ, bound to the C-terminal of GKAP (blue), based on PDB ID 1Q3P. Secondary structure elements are colored yellow for beta-strands and magenta for alpha-helices. Locations of point mutations are circled red and labelled. **(C)** Schematic representation of the Shank1 PDZ ligand binding pocket, with variable sidechain bonds depicted with black triple lines. Note that not all of the variable bonds are present in all peptide binding interactions. The nonpolar interactions of P(0) and the hydrogen bond of P(-2) are highly conserved. The carboxylate interaction is only relevant in terminal motifs, while P(+1) is only found in internal motifs, therefore they are depicted in lower opacity to reflect that. **(D)** Secondary structure composition of the Shank1 PDZ, with multiple sequence alignment comparing it to other PDZ domains. Identities and similaties within 80% are highlighted with red and light red respectively. Note that the β2-β3 loop segment is only found in the Shank PDZ domains. Positions that participate in binding according to currently known experimental structures of the Shank1 PDZ and/or are affected by mutations are marked, with legend included. **(E)** Histogram of mutations from the COSMIC database, overlaid onto the Shank1 PDZ sequence. The mutations analyzed in this study are labelled. **(F)** Partner peptides analyzed in this study, with binding motif amino acids colored according to their properties.

4 Materials and methods

4.1 Selection of mutations and interaction partners for the study

The only ASD associated missense mutation on the PDZ domain of Shank1, the R736Q variant, had been described by Sato *et al.* [10,19] Other cancer associated somatic variants were collected from the COSMIC database. [18] In this case, the four most frequent variants (at the time of data collection) of the region were chosen for the study. Where multiple variants were documented at the same position, the most frequent was picked. The C-terminal peptide of GKAP was chosen as the first model system as it is the most studied, and the additional peptides were chosen with the following considerations: diversity in binding motifs; diversity in associated GO terms; preference for ligands with existing experimental structures in complex with the Shank1-PDZ; preference for ligands with K_d values known from literature. Peptides for experiments were designed based on the works of Zeng et al., Ali et al., Lee et al. [3,5,6]

4.2 Expression of constructs

The wild type Shank1 PDZ domain and its missense variants as well as the 186 amino acid long C-terminal segment of GKAP (GKAP GH1) were expressed in *E. coli* strain. The Shank1 PDZ construct spans from G654 to K768 on the human Shank1 reference sequence (NP_057232.2, Q9Y566-1). A rat Shank-1 ORF plasmid (kindly provided by Enora Moutin from the University of Geneva) was used to amplify the insert for cloning. Note that in this region, Rat and Human ORFs code for the same protein sequences. The insert was ligated into NdeI and BamHI sites of a modified pET-15b vector (Novagen) that contains a tobacco etch virus (TEV) protease cleavage site instead of the thrombin sequence. The expressed construct is equipped with an N-terminal 6xHis tag. Missense mutations were introduced into the Shank1 PDZ plasmid by site directed mutagenesis using PCR primer pairs bearing the desired mutation for the amplification of the whole plasmid. The construct coding the C-terminal segment of GKAP (GKAP GH1) corresponds to the rat GKAP1a D481-L666 region (Uniprot P97836-5) and its insert was picked up from a rat GKAP1a ORF template kindly provided by Enora Moutin. This 186 amino acid long segment differs from the human GKAP sequence of 792-977 only at K501 (Uniprot P97836-5), the human protein (Q9D415-1) has a glutamine amino acid at this position. This insert was ligated into the same modified pET-15b plasmid as used for Shank1 PDZ. The GKAP construct labelled CT43 is 100% identical to the human sequence covering residues 935-977 and was created using the same methods. Constructs coding 12 amino acid long peptides incorporating the binding motifs of GKAP, βPIX, ARAP3, mTOR and ATG13 were designed based on the human protein sequences (Uniprot entries Q9D415-1, Q14155-1, Q8WWN8-1, P42345 and O75143-1 respectively), using peptides listed by Ali et al. as a template. [17] In vitro mutagenesis was used to introduce the sequences into a pGex-4T1 vector, resulting in a GST-tagged construct containing a thrombin site ***(Table S1)***.

4.3 Protein purification

Protein expression from all constructs were induced in BL21 (DE3) cells (Novagen) with 1 mM IPTG at 4 MFU cell density and the recombinant proteins were expressed at 20 °C for 16 h in LB medium. Cell pellets were lysed by ultrasonic homogenization in 10% cell suspension using a lysis buffer (50 mM NaPi, 300 mM NaCl, pH 7.4). After homogenization, cell supernatants were purified by IMAC using 5 ml Nuvia™ Ni-affinity column (Bio-Rad), followed by His-tag removal from Shank1-PDZ proteins with TEV protease. Proteins were further purified by ion exchange chromatography, using 5 ml High Q column for Shank1-PDZ constructs (recombinant Shank protein was collected in the flow through fraction) and High S columns for the GKAP GH1 construct (recombinant GH1 was eluted by NaPi buffer with 1 M NaCl). Protein samples were concentrated by ultrafiltration using Amicon® Ultra

Centrifugal Filter with 3 kDa molecular weight cut off value, and the buffer of recombinant proteins was changed to low salt NaPi Buffer (50 mM NaPi; 20 mM NaCl, 0.02% NaN3; pH 7.4). The concentration of the proteins was measured by their absorbance at 280 nm using a NanoDrop2000 photometer, while their purity and exact molecular weight was analyzed by SDS-PAGE and LC–MS. Before pull-down and BLI assays, Shank1 PDZ constructs were purified additionally by reverse IMAC (the protease-treated sample is loaded onto an IMAC column - the cleaved protein remains in the flowthrough fraction) in order to get rid of trace amounts of His-tagged protein and peptide impurities. In the course of this step 20 mM of imidazole and 0.02% Tween 20 as well as 30 µl of equilibrated Nuvia™ IMAC resin was added to every mg of IEC purified PDZ samples followed by a 2 min RT incubation with gentle but thorough mixing. The beads were sedimented by centrifugation, and the flow-through was retained. The production of the GST-tagged 12 amino acid peptide constructs was identical up to the purification steps. Cell lysates were then loaded onto a Bio-Rad Poly-Prep® Chromatography Column filled with Cytiva Glutathione Sepharose™ 4B beads. The aforementioned low salt NaPi Buffer was used for the binding step, and the same buffer with additional 20 mM glutathione was used to elute the proteins. No additional steps were used for these constructs because sample purity was sufficient and the glutathione content in the buffer was negligible at the dilutions used for later experiments.

4.4 Pull-down experiments

For pull-down assays, the 6xHis-tagged GKAP-GH1 construct was used as the bait and the Shank1-PDZ wild type or its mutants lacking the His-tag was the prey molecule. The proteins were purified for the assay as stated above. All steps of the protocol were performed in PD buffer (50 mM NaPi; 20 mM NaCl; 0.1% Tween 20; 0.1% BSA; 20 mM Imidazole; pH 7.4). For each reaction, a pellet of 20 µl 50% suspension of Nuvia IMAC beads equilibrated in PD buffer was mixed with 70 µM GH1 protein diluted in 40 µl of PD buffer followed by a 2 min. RT incubation with mild shaking. In case of GH1- WT+ control sample 40 µl of PD buffer was added without GH1 protein. After the incubation, beads were washed 3 times with 150 µl of PD buffer and 75 µM Shank1-PDZ diluted in 30 µl PD buffer was mixed with the pellet of beads. In case of GH1+ Shank1-PDZ – control sample PD buffer was added without Shank1-PDZ protein, while wild type Shank1-PDZ was added to the GH1- WT+ control sample. Addition of the prey was followed by a 2 min. RT incubation and three wash steps, then 20 µl of elution buffer (0,5 M Imidazole in PD buffer) was added to the pellet of beads. After a 2 min. RT incubation with mild shaking, 15 µl of 3x Laemmli buffer was added to the samples followed by an additional 2 min. shaking incubation. SDS-PAGE images were analyzed with ImageJ. [20]

4.5 Biolayer Interferometry

Prior to experiments, all Ni-NTA biosensors (Fortebio, USA) were hydrated in kinetic buffer (50 mM NaPi pH 7.4, 20 mM NaCl, 20 mM imidazole, 0.1% BSA, 0.02% Tween 20, 0.02% N3Na) at 25°C for 10 min. The ligand, the 6xHis-tagged GH1 or CT43 protein was immobilized on the surface of the biosensor at a 5 µg/ml concentration in kinetic buffer for 120 sec. The initial baselines were then recorded in kinetic buffer for 30 s using a BLItz system (ForteBio, USA). The association and dissociation sensorgrams of WT and mutant PDZ domains at concentrations ranging from 0.5 µM to 4 µM were recorded for 30 sec each in kinetic buffer, too. The equilibrium dissociation constant (K_d) was determined from the BLI data at various concentrations of the PDZ domains using the global fitting method provided in the BLItz data analysis software. The BLI experiments with the anti-GST biosensors were conducted nearly identically, with the following exceptions. Imidazole was omitted from the kinetic buffer. The GST-tagged proteins were diluted to 20 µg/ml, and the PDZ domains were measured at concentrations ranging from 1.25 µM up to 60 µM. Association and dissociation steps were extended to 60 s.

4.6 Fluorescence polarization spectroscopy

Interaction of FITC-labeled CT12 GKAP peptide (FITC-IEIYIPEAQTRL, BioBasic) with the wild type and mutant Shank1-PDZ samples were measured in kinetic buffer (50 mM NaPi pH 7.4, 20 mM NaCl, 20 mM imidazole, 0.1% BSA, 0.02% Tween 20, 0.02% N3Na) at 25°C. Series of 1.7 fold dilutions of the PDZ domains were prepared (70 µl of sample into 100 µl of kinetic buffer) with 50-150 µM starting concentrations. The concentration of the FITC-C12 peptide was 10 nM constant in all samples except the reference blank sample, where no peptide was added. Fluorescence polarization of the samples was measured in a black, flat 96 well plate (Greiner bio-one) in duplicates (100 µl / rxn) using a Spark 20M multimode microplate reader (TECAN) in filter mode. No Shank was added in the Reference samples, while in the Reference blank there was neither Shank, nor peptide. G-factor was estimated to be 1.067. The equilibrium dissociation constants (K_d) were calculated from the inflection point of the fitted titration curves.

4.7 Thermal shift assay

Shank1-PDZ protein samples were analyzed in 0.2 µg / µl final concentration in low salt NaPi buffer supplemented with Sypro Orange dye in 5x final concentration. Duplicates of 25 µl samples were analyzed in a PikoReal real-time PCR instrument. The temperature was elevated from 15 °C to 90 °C with a 1 °C / 30 sec increment followed by 30 sec incubation and data collection protocol. Fluorescent data was collected in the SybrGreen channel. The negative derivative of the RFU was plotted as a function of temperature in order to get melting temperature values as the peak of the melting curves.

4.8 ECD spectroscopy

Wild type and mutant Shank1-PDZ proteins were measured by ECD spectroscopy using JASCO J-1500 spectrometer (JASCO Corporation, Tokyo, Japan). All samples were diluted to 7 µM in low salt NaPi buffer. ECD spectra were recorded at 30 °C using 0.1 cm path length J/21 quartz cuvette (Jasco Corporation) and 300 µl sample with the following settings: 195–260 nm spectral range, 50 nm/min scanning speed, 1 nm bandwidth, 0.2 nm step size, 0.5 s response time and 3 scans of accumulation and baseline correction. For melting experiments, temperature scan measurements were carried out with the same settings above. Full ECD spectra were recorded at increasingly higher temperatures starting with 30 °C up to 70 °C in 5 °C increments. Thermal denaturation of the protein samples was demonstrated by the decrease of CD values at 200 nm and the increase at 210 nm, since these changes reflect the increase in the proportion of random coils.

4.9 Peptide docking

The WT and mutant PDZ domains in complex with a C-terminal peptide "EAQTRL" of GKAP and apo PDZ domains were modelled in UCSF Chimera 1.18 [21] using MODELLER [22] [ref] and refined with FoldX [23], using structure 1Q3P from the PDB as a starting point. These structures were then used as templates for docking simulations. Peptides were docked using AutoDock Crankpep. [24] First, a structural model for the WT domain in its apo form was created as described above, then the peptides "EAQTRL", "WDETNL" and "DTSTSFS", corresponding to GKAP, βPIX and ARAP3, respectively, were docked into this model, and then compared to the experimental structures available under the PDB IDs 1Q3P, 3QJM and 7A9B, respectively. For more details on PDB structures and constructs, see ***Table S1***. RMSD scores between corresponding structures were calculated in UCSF ChimeraX 1.8 [25], with sidechains compared only up to the Cβ atoms. This is due to the ADCP output producing incomplete ligand sidechains, where each sidechain is represented by only a Cβ-Cγ pair with varying length of the covalent bond to represent volume. These RMSD scores remained below <1 Å for all three complexes, therefore we concluded that the method reproduces the experimentally determined bound conformations sufficiently well. Then, the remaining two peptides were docked into the same model ("EESTRFY" of

mTOR and "VCTTSFS" of ATG13) and all docking calculations were repeated for each of the PDZ mutants.

4.10 Molecular dynamics simulations and analysis of structural ensembles

Explicit solvent molecular dynamics simulations of WT and all mutants paired with each ligand peptide (adding up to 30 simulations altogether for 6 PDZ variants and 5 peptides) were performed with GROMACS [26] on the Komondor supercomputer. The AMBER99SB-IDLN force field was used, with a box setting of 1.0 n minimum distance. An 1000 ns time interval was simulated (for each complex), from which, 500 snapshots were taken. The snapshot ensembles were visually inspected in Chimera 1.8. [21] Structural alignment of the ensembles and RMSD calculations were done with LSQMAN. [27] Secondary structure composition and sidechain solvent accessibilities were calculated with DSSPCont. [28] HBPlus [29] was used to extract lists of possible H-bonds, defined as 4 Å. To calculate specific atom-atom distances and solvent accessibility (to quantify nonpolar interactions), salt bridges, cation-π interactions and X torsion angle distributions, in-house Perl and Python scripts by Z. Gáspári and Z. Kálmán were used. Additionally, FoldX [23], PDBePISA [30] and CaPTURE [31] were used on some individual snapshots for further verification of findings. Principal component analysis was conducted using the ProDy package. [32]

4.11 Evaluation and visualization of data

DNA constructs were designed in SerialCloner 2.6.1. (RRID:SCR_014513). Sequence alignment was performed in BioEdit. (RRID:SCR_007361) [33] PCA modes were inspected in VMD. [34] Other data was evaluated and visualized using Microsoft Excel. An Excel Solver add-in was used for sigmoid curve fitting of FP and CD measurements. [35] Figures were edited in Microsoft Powerpoint.

5 Results

5.1 The most frequent somatic and ASD-associated mutations affect positions around the ligand-binding pocket

Somatic mutations for this study were picked from the COSMIC database, originally with the intent of preferring binding-site mutations for experimental investigation.. Crystal structures 1Q3P, 3QJN (and 3L4F), 7A9B, 6YWZ and 8S1R (which display Shank1 PDZ in complex with GKAP, βPIX, ARAP3, a modified synthetic construct based on GKAP, and a synthetic peptide with sequence similarity to mTOR, respectively) were used as references to analyze the context of each mutation [2–5,36,37]. First, it was noted that the binding site is indeed a hot spot for mutations, and the most common missense mutation spots were located on either the β2 strand or the α2 helix forming its main parts. Four mutations fitting this criteria were picked. The one mutation picked from a study on ASD is also located in this area and has two entries in COSMIC. ***(Fig. 1E)*** [10,18]

The most common mutation according to the COSMIC database, R743H, is documented to interact only in some structures. In its close proximity, the C-terminal residue P(0) of the ligand is buried within a hydrophobic pocket formed by F674, F676 and I742, which is partially covered by R743, which simultaneously also might form a salt bridge with the peptide backbone at P(-1), however this was only observed in some models. [3,5] We predict that a mutation to histidine, a sidechain with less charge and volume, could unfavourably affect these interactions. Another possibility is a transient interaction which was seen only in the study about 6YWZ, the structure containing a synthetic GKAP-based ligand, so far. This interaction involves an acylhydrazone fragment component at the same position as P(-5), for which, R743 competes with R736 and R679. [36]

Residues 677 and 679 are both on the β2 strand, and both bear side chains that were either documented to interact with ligands, or are in close proximity to a known interaction.

V677 in the WT is surrounded by P(-1) and P(-3) of the ligand, both of which are possibly part of the binding interface in most of the complexes. Ligand positions P(-3) and P(-5) form various interactions with R679 in all known structures, including the aforementioned dynamic, transient interaction with the synthetic, GKAP-based ligand. [2,3,5,7,36,37] These two mutations are the closest to the β2-β3 loop in the sequence, a highly mobile segment unique to and conserved in Shank PDZ domains. [3]

The G734S mutation is located right before the α2 helix. It is in similarly close spatial proximity to the β2-β2 loop as position 679, and is next to residue H735 which H-bonds to the conserved Thr P(-2). [2]

R736Q is unique among the mutations in this study as the only one that was known to be associated with ASD, although entries are also documented in the COSMIC database. [10,18] The sidechain is on the surface and there is no data supporting that it contributes to any binding interactions with known partner proteins, although it was observed to interact with the aforementioned synthetic ligand based on the GKAP peptide, along with R743 and R679. [36]

5.2 Missense mutations affect the stability but not the structure of Shank1 PDZ

ECD spectra recorded at 30 °C suggested a well folded, globular structure with beta sheet predominance that is in accordance with the available X-ray structure of the domain (PDB ID 1Q3O [2]) and PDZ domains in general. No significant changes in the ECD spectrum at 30 °C were observed in any of the mutated structures. ***(Fig. 2A)*** However, remarkable differences were detected in their thermal stability both by thermal shift assays (TSA) and CD scan measurements. ***(Fig. 2B, 2C, Table S2)*** Melting points observed by TSA were found to be 59 °C for the WT, and 56.9, 52.0, 58.2, 61.6 and 58.8 °C for the V677M, R679W, G734S, R736G and R743H mutants, respectively. ***(Fig. 2B, 2C)*** These are in good accordance with the CD scan measurements. (***Table S2, S3)*** Both the decrease at 200 nm and the increase at 210 nm in the CD signals by the heating suggests the increase of the proportions of random coil and beta structural elements in the domain.

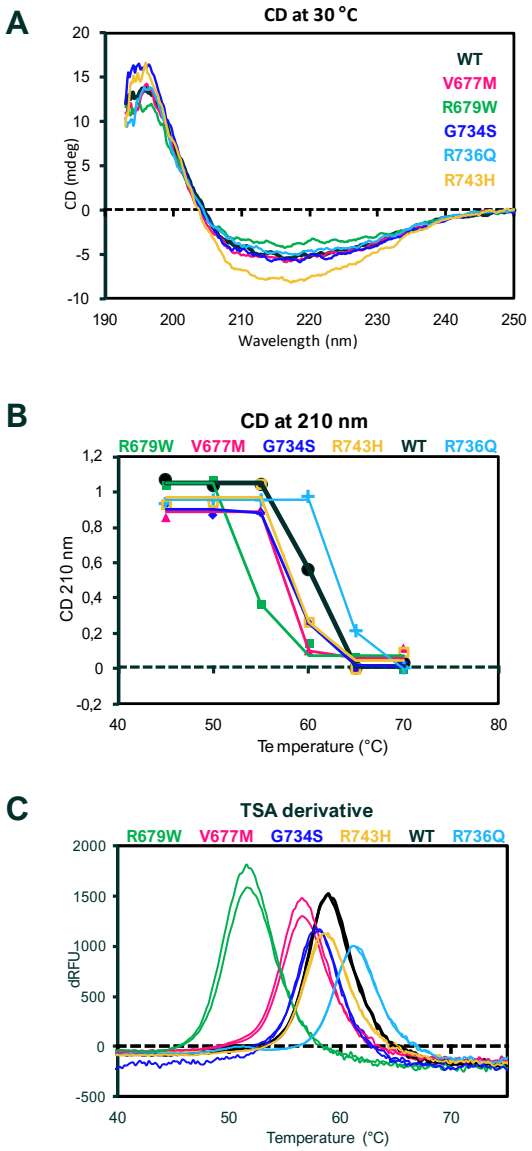

Figure 2. Structural stability of the Shank1-PDZ point mutants. (A) CD values at 30°C. Note that the curves are nearly identical. **(B)** Normalized CD curves of the PDZ isoforms at 210 nm. Note that the inflection points of the curves align with the peaks in the TSA data below, indicating that the results from the two methods are consistent. **(C)** Thermal shift assay results of the different Shank1 PDZ isoforms. Peaks indicate melting points.

5.3 Effect of the mutations on domain stability and GKAP binding move in parallel

In order to examine the functional effect of the mutations, interaction of the wild type and mutant PDZ domains with the GKAP C terminal GH1 construct was tested by a simple pull-down assay. ***(Fig. 3A)*** The R679W variant was pulled down in significantly less amount by GH1 bait than the other variants, for which these experiments showed little difference relative to the wild type. This result was corroborated by fluorescence polarization spectroscopy measurements. Using a 12 amino acid long, FITC labeled GKAP C terminus peptide ligand (Ct12), the dissociation constants (K_d) of WT, V677M, R679W, G734S, R736Q and R743H mutants was calculated to be 5.4-, 13.5-, 59.7-, 8.4-, 2.9- and 6.7 μM respectively, indicating a more than tenfold difference between the affinity of the WT and the R679W variant. ***(Fig. 3B, Table S4)*** Highly similar ratios were obtained by biolayer interferometry, although with slightly lower measured K_d values, 1.5 and 14.5 μM for WT and R679W respectively. ***(Fig. 3C, Table S4)*** Taking into account the results of all methods, it can be stated that variants R679W and V677M attenuate the interaction with GKAP protein to a notable extent. ***(Table 1)***

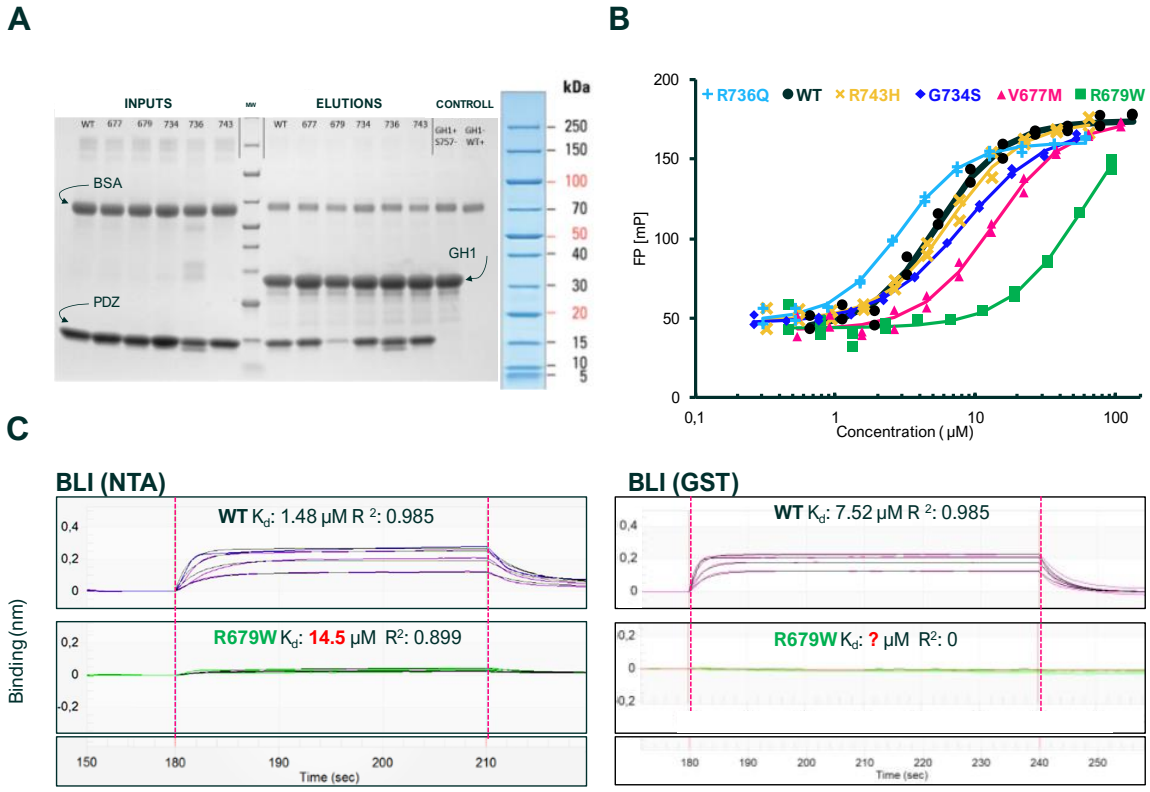

Figure 3. Interaction results with the GKAP partner protein. (A) SDS-PAGE of the pull-down assay which allowed for quantitative measurement of relative binding affinities.**(B)** FP results with fitted curves for all mutants. **(C)** Examples of BLI datasets with fitted curves and resulting K_d values and R2 values describing fitting quality. Note the similarities in curve kinetics and biolayer thickness in the respective experiments.

Remarkably, the ligand binding ability of Shank1 PDZ domain moves in parallel with the effect of the mutations on the stability: the V677M and R679W mutants both exhibit a weaker interaction and a lower T_m than the WT domain, whereas the R736Q variant forms a slightly stronger interaction and has a higher T_m. ***(Fig. 4A)***

	ΔAUC (gel) (%)		**K_d (FP) (μM)**		**K_d (BLI-NTA) (μM)**		**K_d (BLI-GST) (μM)**	
WT	21	***1***	5.4	***1***	1.5	***1***	7.52	***1***
V677M	37	***1.8***	13.5	***2.5***	6.7	***4.5***	62.6	***8.3***
R679W	84	***4***	59.7	***11.1***	14.5	***9.7***	NA	***NA***
G734S	47	***2.2***	8.4	***1.6***	1.7	***1.1***	52.4	***7.0***
R736Q	16	***0.8***	2.9	***0.5***	2	***1.3***	1.79	***0.2***
R743H	25	***1.2***	6.7	***1.2***	1.4	***0.9***	27.3	***3.6***

Table 1. Summary of all binding affinity data obtained with Shank1-PDZ mutants and GKAP. Relative binding affinities are listed next to each data column in bold italic.

5.4 Binding affinity changes of the weaker binders exhibit varying correlations with domain stability

In order to investigate the partner binding of Shank1 PDZ mutants with other partners, we established a BLI-based protocol using GST-tagged peptides. First, we confirmed that the GST-GKAP-CT12 construct produced similar K_d values to those obtained with FP and NTA-BLI as described above. ***(Table 1, Table S4)*** We observed the very same trends but the absolute K_d values appear to be higher than the NTA-BLI results, leading to amplified differences between the variants. As a result, the most unstable mutant, R679W did not produce measurable binding with any of the peptides, therefore no K_d values were obtained for it. For all peptides, the relative K_d values with respect to the WT domain agree well with those reported by Ali et al., with a correlation coefficient of 0.99, but the absolute values are tenfold higher. ***(Table 2)*** We conclude that regardless of these discrepancies stemming from the different methodologies, the relative values within our model system were retained and therefore relevant.

All the peptides turned out to be weaker binders to the wild type PDZ than GKAP, in the following order: βPIX (23.23 uM), ARAP3 (35.76 uM), ATG13 (39.15 uM) and mTOR (720 uM), with the last being significantly, over one order of magnitude weaker than the others. The strongest binder after KAP is βPIX, the only other C-terminal peptide. Generally, the destabilizing mutations exerted a destabilizing effect on the interactions, with the mutants V677M, G734S and R743H consistently producing higher K_d values than WT in all experiments. However, the different mutations affected the binding of the peptides in a highly variable manner. For example, R743H, which binds GKAP only slightly weaker than the WT variant, was shown to be the second weakest binder to βPIX after V677M, and produced similar results to V677M and G734S for the ARAP3 interaction. Even more intriguing are the results with R736Q, the mutant with the highest thermal stability and GKAP-binding affinity: for most peptides the R736Q variant is a weaker binder than the WT, and even with ATG13 it was merely on par with WT. In summary, the correlation observed between thermal stability and GKAP-binding did not apply to any other of the investigated peptides. Overall, the trends indicate that higher destabilization is accompanied by weaker binding, but there is considerable variability between the ligands. ***(Fig. 4A)***

	K_d (ITC) Zeng *et al.* [6] (μM)	**K_d (ITC) (Im *et al.* [4]) (μM)**	**K_d (MST. FP) (Ali *et al.* [5]) (μM)**	**K_d (BLI-GST) (μM)**	**K_d (ITC) (μM)**
GKAP	5.81			**7.52**	**0.45**
βPIX		2.6	0.79	**23.23**	
ARAP3			*3.65	**35.76**	
ATG13			3.8	**39.15**	
mTOR			84	***812.5**	

*value averaged from two different results obtained by same group each

Table 2. Summary of K_d values with various peptides and WT Shank1-PDZ.

A

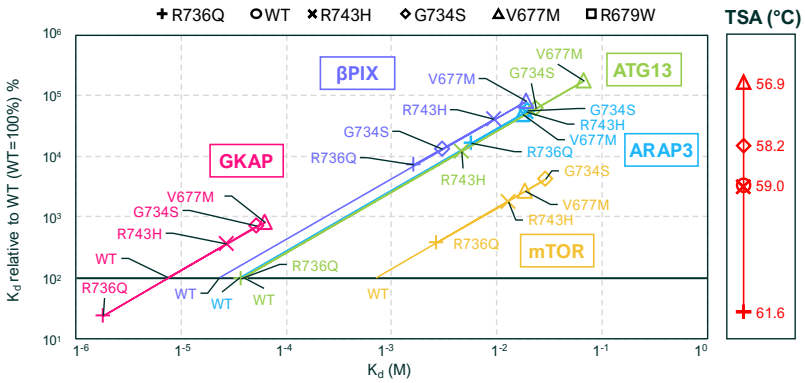

B

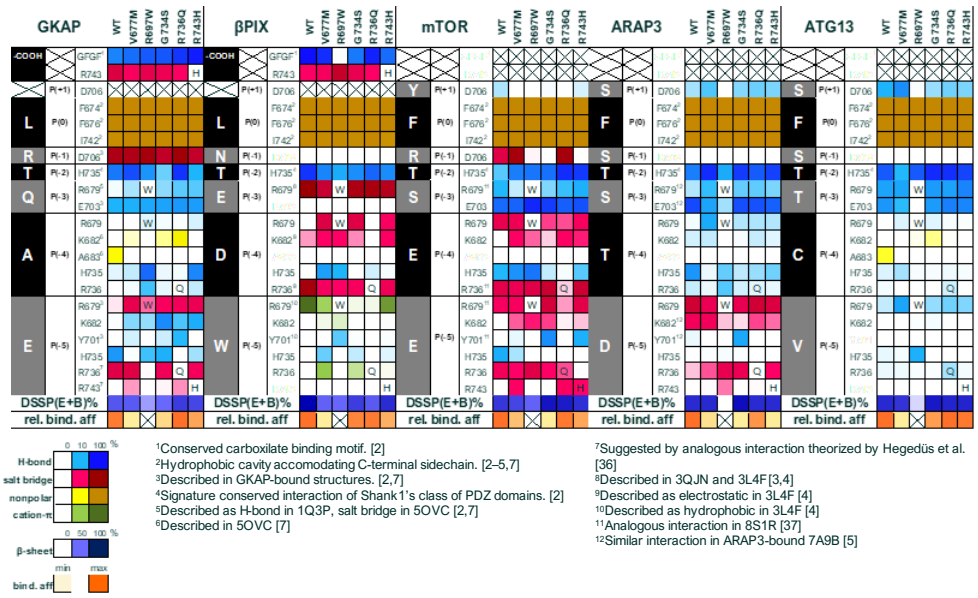

[1]Conserved carboxilate binding motif. [2]
[2]Hydrophobic cavity accomodating C-terminal sidechain. [2–5,7]
[3]Described in GKAP-bound structures. [2,7]
[4]Signature conserved interaction of Shank1's class of PDZ domains. [2]
[5]Described as H-bond in 1Q3P, salt bridge in 5OVC [2,7]
[6]Described in 5OVC [7]
[7]Suggested by analogous interaction theorized by Hegedüs et al. [36]
[8]Described in 3QJN and 3L4F [3,4]
[9]Described as electrostatic in 3L4F [4]
[10]Described as hydrophobic in 3L4F [4]
[11]Analogous interaction in 8S1R [37]
[12]Similar interaction in ARAP3-bound 7A9B [5]

Figure 4. Interactions with βPIX, mTOR, ARAP3 and ATG13. (A) Relative and absolute K_d values of all mutants and peptides. For a table of full series of values, refer to the Supplementary Tables. **(B)** Tables representing all PDZ sidechain to peptide sidechain/backbone interactions in our models. For a full collection of exact values refer to the Supplementary Tables.

5.5 Docking calculations accurately reproduce available experimental structures with wild-type Shank1 PDZ

To rationalize the peptide-specific changes in the interactions with the mutant Shank1 PDZ variants, we performed computational modeling of the PDZ:peptide complexes. Docking simulations were performed and it was determined that those models which have corresponding experimental structures available in the PDB (the GKAP, βPIX and ARAP3 complexes) reproduced the peptide backbone conformations and sidechain orientations observable in said structures. ***(Table S5)*** However, these models were not suitable for detailed sidechain-sidechain interaction analysis, due to the incomplete side chains in the docking output necessitating repair steps which could potentially distort their conformations. Moreover, structural dynamics are known to play an important role in the Shank1 PDZ, which is not incorporated into these static models.

5.6 MD simulations provide a good approximation of experimentally determined stability

To analyze the PDZ:peptide interactions in more detail, MD simulations were performed on all mutant-peptide combinations, using the models created with docking as the starting point. All complexes remained stable during the simulations, with no significant changes in the overall fold of the PDZ domain, with partial peptide dissociation only occurring for some R679W complexes, which is in agreement with the experimental results suggesting it to be the weakest binder. Secondary structure elements as assessed by DSSP remained highly similar to known Shank1 PDZ structures. ***(Table S6)*** Overall, backbone RMSD scores for the full PDZ domains remained low throughout the simulations, rarely exceeding 0.3 Å. A weak correlation to stability was observed, with the least stable mutant, R679W scoring the highest on average. The lowest RMSD was observed for the β-strands, while the α-helices and especially the loops showed higher mobility, as expected. ***(Table S7)*** The peptides exhibited a varying degree of β-strand propensity and low mobility at their conserved P(0)-P(-2) segment and increased dynamics towards the N-terminals. ***(Table S8)*** The intradomain salt bridge network of the apo mutants was not affected significantly, with the exception of the R679W mutant where the strong R679-E703 salt bridge is disrupted. ***(Table S9)*** Next, to analyze the PDZ:ligand bond network, we extracted the interactions of the PDZ side chains to peptide side chains and backbone, and omitted references to backbone-backbone interactions, unless necessary, as the presence of a backbone-backbone H-bond network in the extended β-sheet binding mode is trivial, and is also redundantly represented by β-strand DSSP annotations. ***(Fig. 4B, Table S10)***

5.7 The β2-β3 loop explores different conformations in the complexes

The long, flexible β2-β3 loop is unique to the Shank PDZ domains, and it explored a large conformational space during our simulations and exhibited characteristic differences for the various mutants and peptides. NMR chemical shifts indicated the presence of a short helical segment in the free domain [38], and our DSSP analysis of the MD trajectories reveals that this region shows variable helical/turn character, usually below 50%. Helical propensity is typically lower in the complexes than in the apo form, with the notable exception of most GKAP-bound forms, among other specific cases. ***(Fig. 5A, Table S6)***

To capture a more comprehensive picture of loop conformations, we performed principal component analysis (PCA) on the MD trajectories. PCA analysis of the full PDZ domains revealed that the most important motional modes affect the terminals and the loop regions, predominantly, the β2-β3 loop, thus, considering that the terminals do not participate in binding in these models, we conducted a PCA analysis on the β2-β3 loop (residues 680-700) in isolation. The first principal component (PC) corresponds to the moving "away-towards" of the segment covering the short helical region (residues 683-685) from the PDZ 'core', corroborating our observations on the conformational changes in this region upon binding. Notably, this mode does not correlate with the presence or absence of the

DSSPcont-assigned helix in this region. The second mode affects a somewhat larger region of the loop but is still dominated by residues close to this segment (685-689) and corresponds to an "up-down" type motion when the domain is viewed from the binding site. The third mode is orthogonal to this and affects the middle of the loop and can be described as a "back-and-forth" type rearrangement. ***(Fig. 5B)***

The apo forms of the domain all exhibit similar loop behaviour to each other, with a large overlap of all clusters, with most mutants showing limited mobility with the exception of V677M. However, in the complexes with the GKAP peptide, the loop conformations sample characteristically distinct and relatively compact regions, with G734S, R736Q and R743H almost entirely being separated from the WT along mode 1. The mutant V677M also occupies a region distinct from the wild type, with which only the loop in R679W overlaps.

In the case of the βPIX complexes, the WT variant explores a conformational space only minimally overlapping with any of the mutants. This is likely in correlation with the conformation of P(-5) in the WT, which exhibits a unique cation-π stack with R679 that is diminished in all of the mutans. Notably, the R679W mutant shows the largest variability and is furthest along mode 2 from the WT and also from the other mutants, that are largely clustered together.

The complex formed between the mTOR peptide and the R743H mutant shows the largest variance along mode 1 with two distinct clusters, reflecting the competition between the glutamate sidechains at P(-5) and P(-4), for the same set of sidechain interactions (see below). Similarly, the V677M and WT clusters also contain symmetric subclusters. Other mutants also explore a larger conformational space along this mode, only the WT variant forming a compact cluster similar to that in the GKAP complex.

The β2-β3 loop of the wild-type domain gets highly dynamic upon interaction with the ARAP3 and ATG13 peptides. In the mutants, loop conformations are largely distributed along mode 1 but are still mostly within the range explored in the WT domain. For ARAP3, no clear pattern of similarity to sidechain interactions of P(-5) is discernible, however it is worth noting that Asp P(-5) is another "flip-flopping" sidechain, forming salt bridges with R679, R736 and most importantly, K682. This is the only one out of all peptides in this study which directly binds β2-β3 loop residues with a polar interaction in the WT, which can be a possible explanation to its unique behavior.

The conformational clusters in the ATG13-bound complexes are more compact than for ARAP3, and the preferred loop conformations along the first PC are ordered differently. It should be noted that this peptide partially dissociates from the R679W mutant in the simulations. ***(Fig. 5C, Fig. S2, S3)***

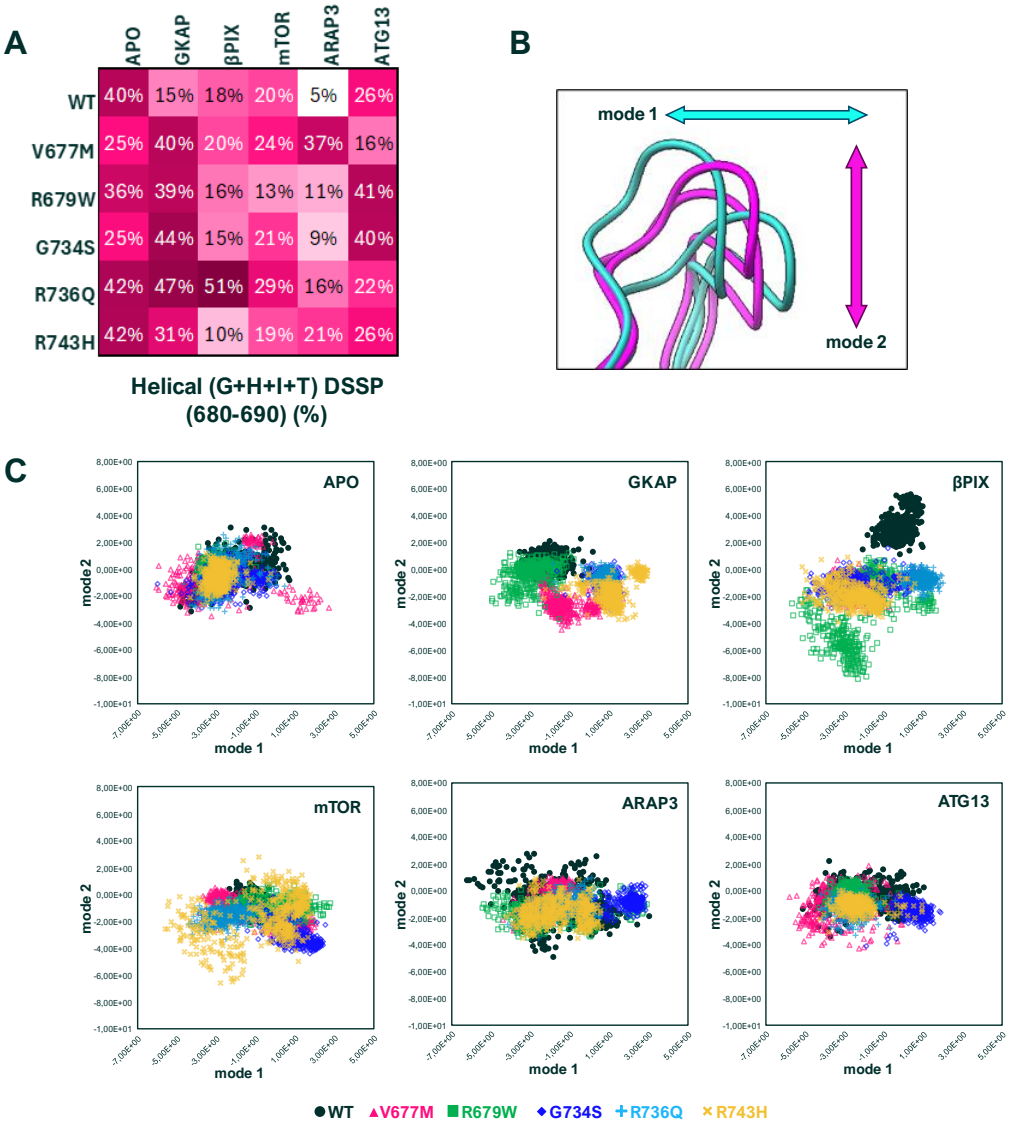

Figure 5. Dynamic properties of the βB-βC loop. (A) Summary table showing the presence of helical DSSP annotations (G, H, I, T) throughout MD simulations as percentage, on the 680-690 segment (βB-βC loop, mobile segment), with proportional color intensity. **(B)** Backbone models representing the first two PCA modes. **(C)** PCA modes 1 and 2 of the βB-βC loop, separated by peptide, colored by mutant.

5.8 A novel role of R743 in carboxylate binding of the C-terminal motifs in GKAP and βPIX

The main-chain carboxyl group of the C-terminal peptides GKAP and βPIX was expected to form a firm hydrogen bond with the conserved carboxylate binding 673GFGF676 motif of the PDZ domain. However, an alternative conformation emerged in our models, where the terminal carboxyl group flips and forms a salt bridge with R743. This observation suggests a novel, important role of the R743 sidechain besides being part of the "arginine triad" capable of binding P(-5), and hydrophobic stacking. The alternative carboxylate-stabilizing interaction of the R743 sidechain was not considered as an important factor in previous known models of the Shank1 PDZ, which made the abundance of the R743H mutation in tumor samples rather elusive. The carboxylate-binding role offers an explanation to this, as well as the weaker binding affinity, since the observed frequency of interactions of the

carboxylate was the lowest in the R743H mutant, as H743 does not form this interaction. ***(Fig. 4B)***

5.9 The Shank1:GKAP complex: alternate interactions of H735 and P(-5) Glu in the WT and altered dynamics in the mutants

Molecular dynamics simulations on the WT domain with the GKAP peptide reproduce most of the previously described residue:residue interactions. PDZ residues F674-F676-L678-I742 form a hydrophobic pocket accommodating P(0) throughout the simulation. Residue D706 forms a characteristic end-on bidentate salt bridge with the P(-1) Arg in ~80% of the simulation frames. However, we did not observe the expected P(-3) Gln or P(-5) Glu interactions with R679, nor a P(-5):Y701 bond and detected only a weak P(-3):E703 interaction. Remarkably, P(-5) Glu forms alternate interactions with R736 and H735, the latter also dynamically changing its side chain orientation to bind to P(-2) Thr instead.

In the mutants, the hydrophobic P(0) interaction, as well as the D706:P(-1) Arg salt bridge remains largely unchanged. The Y701:P(-5) interaction appears in some mutants, most prominently in R736Q, but only to a low extent. In the V677M variant, a relatively stable salt bridge between R679 and P(-5) Glu is formed, despite that, the salt bridges to R736Q were still prominent throughout the simulation, and additional transient salt bridges to R743 formed. x. In the R679W mutant, W679 deforms the binding site while also forming a strong H-bond with the carbonyl O of P(-5) Glu, distorting the extended β-strand structure of the peptide. In the G734Q variant, the H735:P(-2) H-bond occurs only with low frequency, but the alternative interaction formed by H735 can compensate for the loss of it to an extent.

The R736Q variant forms more stable H-bonds and salt bridges with GKAP than the WT domain. The only exception to this is the salt bridge with P(-5) Glu, which forms a transient end-on salt bridge with another arginine of the "triad", R743, while simultaneously establishing an H-bond to Q736, which, we predict, together might compensate for the loss of the salt bridge interaction with the mutated R736. ***(Fig. 6)*** This also explains the increased prevalence of H-bonds between H735 and P(-2), as P(-5) can not establish contacts with this histidine in this mutant. The most prominent change in the R743H mutant is the lack of the aforementioned carboxylate binding interaction of position 743. ***(Fig. 4B)***

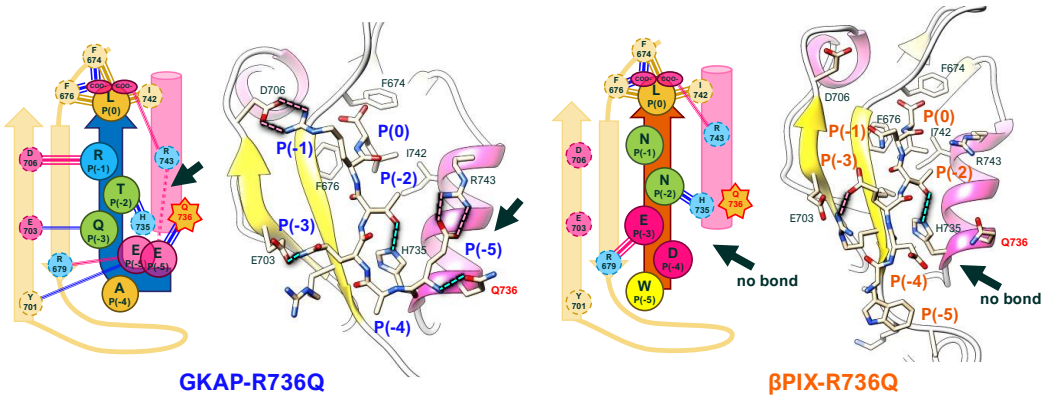

Figure 6. Schematic and 3D models of the R736Q-GKAP and R736Q-bPIX complexes.
In the WT-GKAP interaction, P(-5) forms a salt bridge with R736, which in the mutant is replaced by a transient salt bridge with R743 which results in a strong hydrogen bond with Q736. The analogous interaction to this in the bPIX peptide is the salt bridge between P(-4) and R736 – in the R736Q mutant, this salt bridge is entirely lost and P(-4) does not form alternative bonds. Full a full series of schematic diagrams, refer to the Supplementary Figures.

5.10 Previously unseen cation-π stack in the βPIX interaction varies highly per mutant

The peptide of βPIX exhibits a very stable β-strand conformation in complex with Shank1-PDZ WT but a reduced number of sidechain interactions compared to GKAP. The P(0) Leu remains inserted into the hydrophobic pocket. The H735:P(-2) sidechain H-bond is also more stable, appearing in ~94% of the snapshots, as are the salt bridges formed by Asp P(-4) and Glu P(-3) with R736 and R679, respectively, in accordance with the experimental structure 3QJN and 3L4F. The only major deviation from these X-ray structures is the behavior of P(-5) Trp, which, instead of being inserted into the β2-β3 loop, stacks onto R679 in a cation–π interaction.

In the V677M mutant complex, positions P(0)-P(-2) remain unaffected as expected. In contrast, the P(-3):R679 salt bridge is weakened, as R679 instead forms an intramolecular interaction with E703. This renders P(-5) Trp to transiently stack against R736, competing with P(-4) Asp for this sidechain. This also seems to force the N-terminal part of the peptide out of the binding pocket.

The R679W mutation largely deforms the extended conformation of the bound peptide.

During the simulation of the G734S and the R743H variants, P(-5) Trp undergoes a rearrangement from interacting with a hydrophobic surface formed by the aliphatic segments of A681-Q684 to taking over the interaction with R736 from P(-4) Asp. In this conformation, both P(-4) Asp and P(-3) Glu form a salt bridge with R679, while H735 also flips towards R736, similar to the WT-GKAP scenario.

In the R736Q mutant, the salt bridge between P(-4) Asp and R736 can be considered similar to the one formed by P(-5) Glu in GKAP. However, while Glu P(-5) of GKAP can compensate for the lack of the R679 salt bridge in this mutant, by interacting with R743, P(-4) Asp of βPIX, being shorter, can not participate in an analogous salt bridge. ***(Fig. 4B, 6)***

5.11 A delicately balanced sidechain competition in the mTOR peptide is disrupted in the mutant complexes

Although there is no available experimental structure for the mTOR:Shank1 PDZ complex, the PDB entry 8S1R, featuring a similar internal peptide motif (Ac-$_{[P(-5)]}$EESTSFQGP$_{[P(+3)]}$-CONH$_2$), can be used as a proxy reference. Residue P(0) Phe of the mTOR peptide remains inserted into the hydrophobic pocket, and P(-1) Arg forms a salt bridge similarly to GKAP, albeit with half of the frequency (39.2% vs. 82%). While the frequency of the H735 H-bond with P(-2) Thr is much lower than for GKAP, P(-3) Ser interacts with E703 more frequently than GKAP's P(-3) Gln. Residues P(-5) and P(-4), both glutamates, form competitive interactions with R736 and R679, taking multiple turns over the course of the simulation. In the 8S1R X-ray structure, the sidechains are paired as P(-4)-R736 and P(-5)-R679. Remarkably, H735 prefers forming H-bonds to either of these glutamates rather than to P(-2) Thr.

Similarly to that observed for βPIX, the steric hindrance effect of the V677M replacement is towards P(-3) instead of P(-1). Remarkably, P(-1) is bound to D706 in 90% of the snapshots, a frequency more than twice than observed for the WT domain. Overall, this interaction is characterized by a stabilized C-terminal half and a destabilized N-terminal half of the peptide.

In the R679W mutant, many interactions are missing. The W679 sidechain is unable to form any salt bridges, and P(-1) Arg forms a cation–π interaction with P(+1) Tyr instead

of the salt bridge with D706. The same cation-pi interaction also occurs in the G734S, R736Q and R743H mutants.

In the R736Q mutant, the loss of the ionic interaction between P(-5) Glu and the mutated R736 can only be partially compensated by R743 because of the competition with R679, with which P(-4) Glu can also interact. H735 remains H-bonded to P(-2) Thr, similarly to the R736Q-GKAP interaction. ***(Fig. 4B)***

5.12 H735 exhibits unique alternative H-bond in ARAP3

For this complex, comparisons can be made with the experimental structure 7A9B. While most interactions described for this X-ray structure are observed in our simulations, the H-bond between Ser P(+1) and D706 does not seem to be stably formed neither in the WT domain or any of the mutants. In the wild type complex, P(-3) Ser forms a stable H-bond with E703. The side chain of H735 forms almost equally populated alternate interactions with P(-4) Thr and P(-2) Thr. ***(Fig. 7A)*** The P(-5) Asp forms a salt bridge with R679, and, with low frequency, also with K682.

The V677M mutant exhibits a similar pattern with the notable exception of H735 interacting only with P(-2) and not at all with P(-4). This might be explained by the distorting effect of the mutation on the P(-3)-P(-5) segment of the peptide, also reducing the P(-3):E703 and P(-5):Y701 contacts. Similarly to V677M, the G734S and R736Q mutants also exhibit strong preference for the conserved P(-2)-H735 interaction over P(-4)-H735 with the addition that no salt bridge between K682 and P(-5) is observed. R736Q and G743S also show these same patterns with some slight variations in the P(-5) interactions

The peptide bound to the R679W mutant almost dissociates during the simulation, one of the two cases when such behavior was observed in our study. ***(Fig. 4B)***

5.13 ATG13 binding is dominated by H-bonds and nonpolar interactions

ATG13 is the only analyzed peptide with no similar experimental structure available. The interaction pattern of WT-ATG13 appears to be dominated by H-bonds and hydrophobic interactions throughout the length of the peptide. The C-terminal P(+1) Ser forms a H-bond with D706 only in about 10% of the frames, and P(-1) Ser does not participate in any sidechain interactions. The only additional sidechain H-bond in the whole peptide is formed between P(-3) Thr and R679, with a frequency of about 20%. The hydrophobic residues in the 680-690 segment of the β2-β3 loop are less exposed than in the GKAP complex as they accommodate both P(-4) Cys and partially, P(-5) Val.

The interaction pattern varies only little for most of the mutant PDZ domains. The exception is the complex with R679W in which the peptide which nearly dissociates but remains tethered to the domain by alternative H-bonds of the carbonyl oxygen of P(-3) Thr, P(-4) Cys, as well as the sidechain OG of P(-2) Thr to the imidazole ring of H735.

The V677M mutant exhibits diminished sidechain interactions, most notably the P(-2) Thr:H735 H-bond being almost nonexistent, while the P(+1) Ser:D706 H-bond is more prevalent. ***(Fig. 4B)***

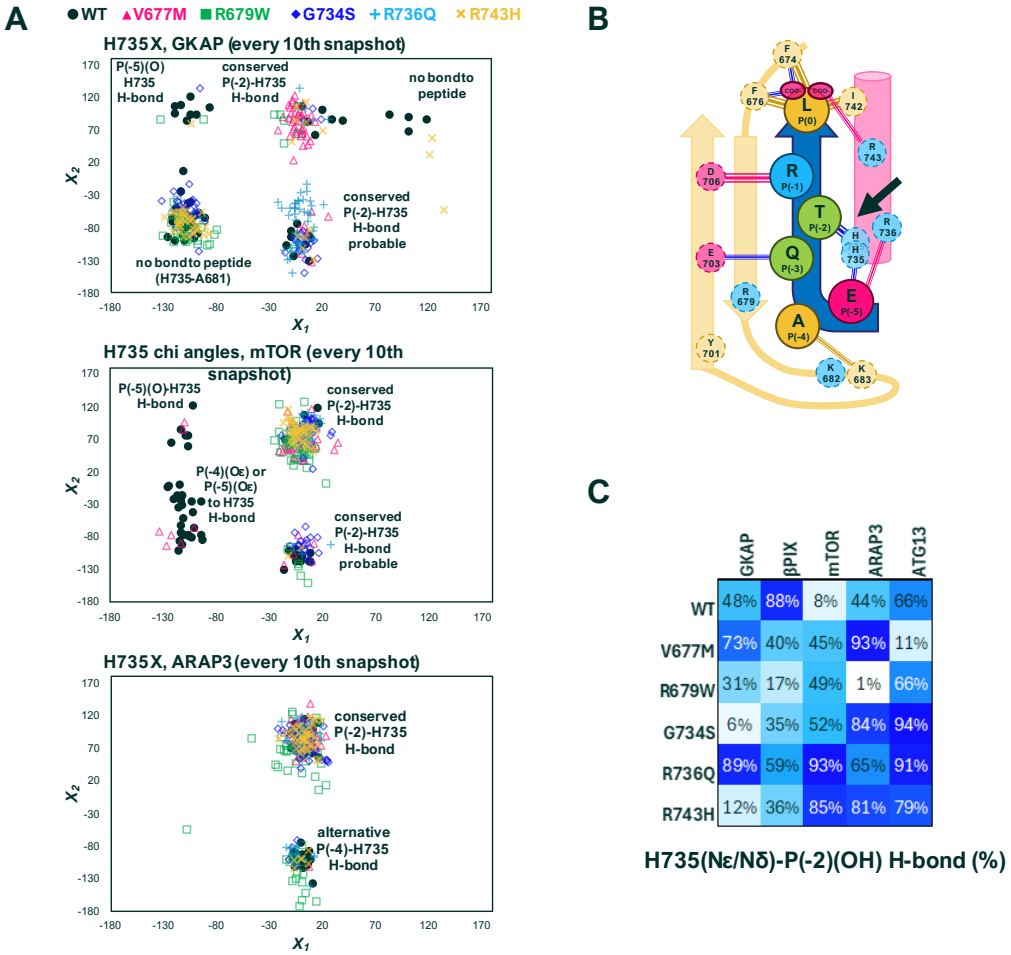

Figure 7. Dynamics of the H735 sidechain. **(A)** X dihedrals explored by the H735 sidechain during peptide binding. Note that the X-axis was shifted by 180° for better visualization. Each cluster is labelled with the sidechain bond that is probable to occur in said conformation. **(B)** Schematic representation of the WT-GKAP binding. Note the alternative H-bond to P(-5) (besides the conserved P(-2) interaction) formed by H735. **(C)** Summary table showing the presence of the conserved H735 H-bond throughout MD simulations as percentage, with proportional color intensity.

6 Discussion

6.1 Overview of the mutations

All of the most frequent Shank1 PDZ mutations listed in the COSMIC database affect binding site residues. Considering that besides the binding site, the β2-β3 loop, unique to Shank PDZ domains, is also highly conserved in the family, this distribution of the mutations is not necessarily trivial.

Moreover, all the affected residues are located on the surface of the domain, with their sidechains pointing towards the solvent. Therefore, the large changes observed in thermal stability were rather surprising as changing these residues is not expected to disrupt internal residue networks. Perhaps a simple but partial explanation can be provided for the R679W mutant where the R679-E703 salt bridge is disrupted. However, the small destabilizing effect of a Gly to Ser change in G734S and the increased stability in R736Q can not be easily explained on the basis of individual residue properties or clearly identifiable interactions. It should be noted that several X-ray structures of Shank1 PDZ

indicate the presence of PDZ dimers [2,3,5,6] that might, in theory, increase the number of residue-residue interactions that should be considered when interpreting mutation effects. Our previous NMR study [38] indicated that the Shank1 PDZ is monomeric in solution, and we have not observed any deviations from the expected molecular mass during protein purification. Thus, although the possibility of dimerization, especially upon ligand binding, cannot be completely dismissed for all variants, we chose to interpret the effects on the monomeric structure as the simplest plausible model.

MD simulations indicated only subtle differences between the global structure of the mutants, with the PDZ domain, with the largest changes observed for the β2-β3 loop. As could be expected, this region showed high flexibility and explored a wide range of conformations, with its helical propensity ranging from 5-51% (G, H, I and T states as assigned by DSSP). ***(Fig. 5A)*** The whole loop, spanning positions 680 to 700, is about one fifth of the length of the canonical domain, while it provides a relatively even larger solvent-accessible surface area, about one fourth of the total of the full PDZ. The mutations that caused the highest instability were V677M, R679W and G734S - the first two being the closest to the loop in the sequence, while 734 being in close spatial proximity in the structure.

6.2 Dynamics of alternating interactions might be a key contributor to ligand selectivity and binding affinity

Molecular dynamics simulations can capture important aspects of the dynamic behavior of biomolecules, but can not necessarily be expected to accurately reflect all aspects of the actual conformational fluctuations and the delicate balance between all interactions, especially for the diverse systems investigated in this work. Thus, we interpret our analysis as a semiquantitative description that can shed light on several important dynamic aspects and possible interactions, but the actual dynamic balance between the observed conformational states might not be precisely captured.

The most remarkable general observation in our molecular dynamics calculations was the presence of a number of competing interactions. Most of these are alternative salt bridges, like the one formed by the C-terminal carboxylate and R743, which, in turn, also can pair with Asp/Glu residues at position P(-5). This is somewhat surprising given the expected distance between residues P(0) and P(-5) in the extended conformation of the peptide, but during our simulations, the overall flexibility of the complex allowed the formation of both interactions by R743.

Another important dynamic interaction is formed by the conserved H735 imidazole side chain with the residues in the peptides in positions P(-2), P(-4), and P(-5). ***(Fig. 4B, 7A-C)*** This interaction varies largely for the different peptides and PDZ mutants, ranging from a highly dynamic scenario in the case of GKAP and WT PDZ, where intramolecular H-bond formation is also observed, to the stable H-bond with residue P(-2) in the complexes with ARAP3 and βPIX. (Fig. 6) The difference in the behavior of H735 with different partner peptides suggests a role of H735 in partner selectivity. This is rather unexpected as H735-P(-2) was believed to be a static interaction with the only role of stabilizing the peptide. It should be noted that our molecular dynamics simulations can not account for the changes of the protonation state of the imidazole ring, which might also contribute to the variability of the interactions.

6.3 Functional equivalence of side chains in different peptides

We have also observed interactions from the peptide side that can more or less replace each other, suggesting the presence of some degree of functional equivalence between sequential positions in the partner peptides. For example, amino acid residues in peptide positions P(-1) and P(+1), typically positively charged ones, are often interacting with the

PDZ residue D706. On the other hand, E703 tends to form an H-bond with P(-3), most commonly a serine in both internal and C-terminal ligands. P(+1), P(-1) and P(-3) tend to always remain pointing towards and interacting with the β-strand side of the binding pocket, a common orientation seen in similar PDZ domains. [39]

Positions P(-4) and P(-5) show considerable variability, but with a preference towards glutamate or aspartate. Side chains in both positions can form salt bridges with the PDZ residues R679 and R736. Hydrophobic sidechains are also common in these two positions, and if present, they are accommodated by the β2-β3 loop. Our simulations suggest that the interactions formed by P(-4) and P(-5) can drastically influence the backbone conformation of the peptide, with a R736:P(-5) interaction consistent with the emergence of a kinked structure, while hydrophobic interactions with the P(-5) position result in altered β2-β3 loop dynamics in the PDZ.

For some of the interactions, the sum of intermolecular sidechain bonds correlates well with binding affinity, highlighting the example of the R736Q mutant: compensatory interactions are formed which restore the stability of the complex in the GKAP interaction, while this phenomenon is not observed during, for example, bPIX binding, resulting in the loss of a significant salt bridge.***(Fig. 6)*** Generally, the beta-sheet propensity of the peptide was also a good reflection of complex stability. However, not all of the simulations can be interpreted in such a straightforward manner. Considering the relatively weak nature of the interactions (micromolar range, even using the measurement techniques that produced the lowest K_d values), it is a possibility that energetic contribution of overall PDZ stability versus the peptide binding network are on par, creating the complex response to the mutations observed in the experimentally determined binding affinities.

Understanding the relationship between binding affinities and mutation induced structural perturbations is further complicated by the apparent dynamic nature of the peptide binding. Several transient, competing interactions were suggested by the MD simulations, including that of the carboxylate and H735, previously considered to be stable interactions due to their conserved nature. This, in addition to the dynamics of P(-5) in relation to R679-R736-R743 that was also proposed by previous studies [ref 6ywz] and the remarkable mobility of the β2-β3 loop paints a picture of a highly flexible complex.

6.4 Possible consequences of the Shank PDZ mutations in associated diseases

All of the partner peptides analyzed in this study have potential or proven connections to disease pathways. Most notably, Shank proteins all have an essential role in regulating postnatal brain development via the Akt/mTOR pathway, however, little is known about the contribution of its individual domains. [8] The GKAP-Shank interaction via the PDZ domain is crucial as it tethers various other PSD proteins to the NMDA receptors, consequently, GKAP is often described as the main interaction partner of the Shank-PDZ. However, the contribution of this complex to the aforementioned growth factor pathway is elusive. [40] Involvement of Shank2 in oncogenesis can be explained, at least in part, by the requirement of the interaction between the Shank2-PDZ and βPIX to regulate Hippo signaling. [11] For the remaining two peptides investigated in this study, we found no direct evidence in the literature on how they influence Shank1 function, however, ATG13 is also a member of the TOR pathway and is involved in autophagy, while ARAP3, similarly to βPIX, is involved in GTPase mediated signaling and regulates cytoskeletal remodeling. [41,42]

Loss of Shank function can be one of the mechanisms behind ASD, as observed in Phelan-McDermid syndrome and experiments with KO and KI mice. [9,43,44] Conversely, overexpression of Shank proteins is oncogenic. [11,14,17] Interestingly, all of the cancer associated mutations analyzed in our study turned out to be destabilizing, loss-of-function mutations, while the one found in also ASD was the mutant with increased stability. However, as the above example with βPIX and the Shank2 PDZ shows, loss or gain of

function in a single domain does not necessarily translate to models of under- and overexpression respectively. Instead, in an interaction network as abundant and complex as the one Shank1 is centered at, the perturbing effects of a mutation might require an explanation within a larger context. Our results show that each disease-associated mutation has its own unique pattern in affecting the five interactions, to which overall domain stability was only a partial contributor. This suggests a highly complex perturbing effect on the interaction network of the domain, with binding preferences shifting from one partner to another in some cases. Systems biology simulations by Miski et al. had recently demonstrated that small changes in the initial conditions, such as a single K_d value, can result in a large perturbation on the PSD interaction network. [45] Experimental data like ours can be used as input to refine such modeling approaches to address similar systems more realistically.

Our results highlight the intricate interplay of residue-residue interactions in partner binding and show that the effects of mutations can be highly partner-specific in the case of a promiscuous partner binding domain. We believe that the complex analysis of multiple affected interactions like our study can contribute to a more comprehensive description of the rewiring of protein:protein interaction networks upon specific mutations, leading to a deeper understanding of the interplay between molecular-level changes and phenotypes.

7 Supplementary files

Besides figures and tables cited in the paper, we also provide a full series of schematic diagrams representing peptide binding modes in Figure S1 found in the SupplementaryFigures.pdf file, as well as additional data derived from MD simulations in Tables S10-16 of the SupplementaryTables.xls file.

8 Acknowledgments

The authors acknowledge the support of the National Research, Development and Innovation Office - NKFIH - through grant OTKA K 137947 (to Z.G.), and the Digital Government Development and Project Management Ltd. for awarding us access to the Komondor HPC facility based in Hungary. The authors express gratitude for the contributions of: Enora Moutin for providing cDNA constructs, Viktor Farkas for the assistance with CD measurements, and Zsuzsanna Stránerné Szabó, Anna Oláh, József Hegedüs and Melinda Keresztes for their contribution to the experiments over the years.

9 References

[1] M. Sheng, E. Kim, The Shank family of scaffold proteins, J. Cell Sci. 113 (2000) 1851–1856. https://doi.org/10.1242/jcs.113.11.1851.

[2] Y.J. Im, J.H. Lee, S.H. Park, S.J. Park, S.-H. Rho, G.B. Kang, E. Kim, S.H. Eom, Crystal Structure of the Shank PDZ-Ligand Complex Reveals a Class I PDZ Interaction and a Novel PDZ-PDZ Dimerization, J. Biol. Chem. 278 (2003) 48099–48104. https://doi.org/10.1074/jbc.M306919200.

[3] J.H. Lee, H. Park, S.J. Park, H.J. Kim, S.H. Eom, The structural flexibility of the shank1 PDZ domain is important for its binding to different ligands, Biochem. Biophys. Res. Commun. 407 (2011) 207–212. https://doi.org/10.1016/j.bbrc.2011.02.141.

[4] Y.J. Im, G.B. Kang, J.H. Lee, K.R. Park, H.E. Song, E. Kim, W.K. Song, D. Park, S.H. Eom, Structural Basis for Asymmetric Association of the βPIX Coiled Coil and Shank PDZ, J. Mol. Biol. 397 (2010) 457–466. https://doi.org/10.1016/j.jmb.2010.01.048.

[5] M. Ali, M.M. McAuley, S. Lüchow, S. Knapp, A.C. Joerger, Y. Ivarsson, Integrated analysis of Shank1 PDZ interactions with C-terminal and internal binding motifs, Curr. Res. Struct. Biol. 3 (2021) 41–50. https://doi.org/10.1016/j.crstbi.2021.01.001.

[6] M. Zeng, Y. Shang, T. Guo, Q. He, W.-H. Yung, K. Liu, M. Zhang, A binding site outside the canonical PDZ domain determines the specific interaction between Shank and SAPAP and their function, Proc. Natl. Acad. Sci. 113 (2016). https://doi.org/10.1073/pnas.1523265113.

[7] S.K. Ponna, S. Ruskamo, M. Myllykoski, C. Keller, T.M. Boeckers, P. Kursula, Structural basis for PDZ domain interactions in the post-synaptic density scaffolding protein Shank3, J. Neurochem. 145 (2018) 449–463. https://doi.org/10.1111/jnc.14322.

[8] J.P.H. Burbach, Unraveling a pathway to autism, Science 351 (2016) 1153–1154. https://doi.org/10.1126/science.aaf5097.

[9] Y. Qin, Y. Du, L. Chen, Y. Liu, W. Xu, Y. Liu, Y. Li, J. Leng, Y. Wang, X.-Y. Zhang, J. Feng, F. Zhang, L. Jin, Z. Qiu, X. Gong, H. Wang, A recurrent SHANK1 mutation implicated in autism spectrum disorder causes autistic-like core behaviors in mice via downregulation of mGluR1-IP3R1-calcium signaling, Mol. Psychiatry 27 (2022) 2985–2998. https://doi.org/10.1038/s41380-022-01539-1.

[10] C.S. Leblond, C. Nava, A. Polge, J. Gauthier, G. Huguet, S. Lumbroso, F. Giuliano, C. Stordeur, C. Depienne, K. Mouzat, D. Pinto, J. Howe, N. Lemière, C.M. Durand, J. Guibert, E. Ey, R. Toro, H. Peyre, A. Mathieu, F. Amsellem, M. Rastam, I.C. Gillberg, G.A. Rappold, R. Holt, A.P. Monaco, E. Maestrini, P. Galan, D. Heron, A. Jacquette, A. Afenjar, A. Rastetter, A. Brice, F. Devillard, B. Assouline, F. Laffargue, J. Lespinasse, J. Chiesa, F. Rivier, D. Bonneau, B. Regnault, D. Zelenika, M. Delepine, M. Lathrop, D. Sanlaville, C. Schluth-Bolard, P. Edery, L. Perrin, A.C. Tabet, M.J. Schmeisser, T.M. Boeckers, M. Coleman, D. Sato, P. Szatmari, S.W. Scherer, G.A. Rouleau, C. Betancur, M. Leboyer, C. Gillberg, R. Delorme, T. Bourgeron, Meta-analysis of SHANK Mutations in Autism Spectrum Disorders: A Gradient of Severity in Cognitive Impairments, PLoS Genet. 10 (2014) e1004580. https://doi.org/10.1371/journal.pgen.1004580.

[11] L. Xu, P. Li, X. Hao, Y. Lu, M. Liu, W. Song, L. Shan, J. Yu, H. Ding, S. Chen, A. Yang, Y.A. Zeng, L. Zhang, H. Jiang, SHANK2 is a frequently amplified oncogene with evolutionarily conserved roles in regulating Hippo signaling, Protein Cell 12 (2021) 174–193. https://doi.org/10.1007/s13238-020-00742-6.

[12] C.-F. Chang, S.-P. Huang, Y.-M. Hsueh, J.-H. Geng, C.-Y. Huang, B.-Y. Bao, Genetic Analysis Implicates Dysregulation of SHANK2 in Renal Cell Carcinoma Progression, Int. J. Environ. Res. Public. Health 19 (2022) 12471. https://doi.org/10.3390/ijerph191912471.

[13] J. Lilja, T. Zacharchenko, M. Georgiadou, G. Jacquemet, N.D. Franceschi, E. Peuhu, H. Hamidi, J. Pouwels, V. Martens, F.H. Nia, M. Beifuss, T. Boeckers, H.-J. Kreienkamp, I.L. Barsukov, J. Ivaska, SHANK proteins limit integrin activation by directly interacting with Rap1 and R-Ras, Nat. Cell Biol. 19 (2017) 292–305. https://doi.org/10.1038/ncb3487.

[14] L. Wang, Y. Lv, G. Liu, The roles of SHANK1 in the development of colon cancer, Cell Biochem. Funct. 38 (2020) 669–675. https://doi.org/10.1002/cbf.3529.

[15] E. Loi, L. Moi, A. Fadda, G. Satta, M. Zucca, S. Sanna, S. Amini Nia, G. Cabras, M. Padoan, C. Magnani, L. Miligi, S. Piro, D. Gentilini, M.G. Ennas, M.C. Southey, G.G. Giles, N. Wong Doo, P. Cocco, P. Zavattari, Methylation alteration of SHANK1 as a predictive, diagnostic and prognostic biomarker for chronic lymphocytic leukemia, Oncotarget 10 (2019) 4987–5002. https://doi.org/10.18632/oncotarget.27080.

[16] X. Liu, M. Yuan, B.W.-M. Lau, Y. Li, SHANK family on stem cell fate and development, Cell Death Dis. 13 (2022) 880. https://doi.org/10.1038/s41419-022-05325-3.

[17] B. Chen, H. Zhao, M. Li, Q. She, W. Liu, J. Zhang, W. Zhao, S. Huang, J. Wu, SHANK1 facilitates non-small cell lung cancer processes through modulating the ubiquitination of Klotho by interacting with MDM2, Cell Death Dis. 13 (2022) 403. https://doi.org/10.1038/s41419-022-04860-3.

[18] Z. Sondka, N.B. Dhir, D. Carvalho-Silva, S. Jupe, null Madhumita, K. McLaren, M. Starkey, S. Ward, J. Wilding, M. Ahmed, J. Argasinska, D. Beare, M.S. Chawla, S. Duke, I. Fasanella, A.G. Neogi, S. Haller, B. Hetenyi, L. Hodges, A. Holmes, R. Lyne, T. Maurel, S. Nair, H. Pedro, A. Sangrador-Vegas, H. Schuilenburg, Z. Sheard, S.Y. Yong, J. Teague, COSMIC: a curated database of somatic variants and clinical data for cancer, Nucleic Acids Res. 52 (2024) D1210–D1217. https://doi.org/10.1093/nar/gkad986.

[19] D. Sato, A.C. Lionel, C.S. Leblond, A. Prasad, D. Pinto, S. Walker, I. O'Connor, C. Russell, I.E. Drmic, F.F. Hamdan, J.L. Michaud, V. Endris, R. Roeth, R. Delorme, G. Huguet, M. Leboyer, M. Rastam, C. Gillberg, M. Lathrop, D.J. Stavropoulos, E. Anagnostou, R. Weksberg, E. Fombonne, L. Zwaigenbaum, B.A. Fernandez, W. Roberts, G.A. Rappold, C.R. Marshall, T. Bourgeron, P. Szatmari, S.W. Scherer, SHANK1 Deletions in Males with Autism Spectrum Disorder, Am. J. Hum. Genet. 90 (2012) 879–887. https://doi.org/10.1016/j.ajhg.2012.03.017.

[20] C.A. Schneider, W.S. Rasband, K.W. Eliceiri, NIH Image to ImageJ: 25 years of image analysis, Nat. Methods 9 (2012) 671–675. https://doi.org/10.1038/nmeth.2089.

[21] E.F. Pettersen, T.D. Goddard, C.C. Huang, G.S. Couch, D.M. Greenblatt, E.C. Meng, T.E. Ferrin, UCSF Chimera--a visualization system for exploratory research and analysis, J. Comput. Chem. 25 (2004) 1605–1612. https://doi.org/10.1002/jcc.20084.

[22] B. Webb, A. Sali, Comparative Protein Structure Modeling Using MODELLER, Curr. Protoc. Bioinforma. 54 (2016) 5.6.1-5.6.37. https://doi.org/10.1002/cpbi.3.

[23] J. Schymkowitz, J. Borg, F. Stricher, R. Nys, F. Rousseau, L. Serrano, The FoldX web server: an online force field, Nucleic Acids Res. 33 (2005) W382-388. https://doi.org/10.1093/nar/gki387.

[24] Y. Zhang, M.F. Sanner, AutoDock CrankPep: combining folding and docking to predict protein–peptide complexes, Bioinformatics 35 (2019) 5121–5127. https://doi.org/10.1093/bioinformatics/btz459.

[25] E.C. Meng, T.D. Goddard, E.F. Pettersen, G.S. Couch, Z.J. Pearson, J.H. Morris, T.E. Ferrin, UCSF ChimeraX: Tools for structure building and analysis, Protein Sci. 32 (2023) e4792. https://doi.org/10.1002/pro.4792.

[26] S. Páll, A. Zhmurov, P. Bauer, M. Abraham, M. Lundborg, A. Gray, B. Hess, E. Lindahl, Heterogeneous parallelization and acceleration of molecular dynamics simulations in GROMACS, J. Chem. Phys. 153 (2020) 134110. https://doi.org/10.1063/5.0018516.

[27] G.J. Kleywegt, Experimental assessment of differences between related protein crystal structures, Acta Crystallogr. D Biol. Crystallogr. 55 (1999) 1878–1884. https://doi.org/10.1107/s0907444999010495.

[28] P. Carter, C.A.F. Andersen, B. Rost, DSSPcont: continuous secondary structure assignments for proteins, Nucleic Acids Res. 31 (2003) 3293–3295. https://doi.org/10.1093/nar/gkg626.

[29] I.K. McDonald, J.M. Thornton, Satisfying hydrogen bonding potential in proteins, J. Mol. Biol. 238 (1994) 777–793. https://doi.org/10.1006/jmbi.1994.1334.

[30] E. Krissinel, K. Henrick, Inference of macromolecular assemblies from crystalline state, J. Mol. Biol. 372 (2007) 774–797. https://doi.org/10.1016/j.jmb.2007.05.022.

[31] J.P. Gallivan, D.A. Dougherty, Cation-π interactions in structural biology, Proc. Natl. Acad. Sci. 96 (1999) 9459–9464. https://doi.org/10.1073/pnas.96.17.9459.

[32] S. Zhang, J.M. Krieger, Y. Zhang, C. Kaya, B. Kaynak, K. Mikulska-Ruminska, P. Doruker, H. Li, I. Bahar, ProDy 2.0: increased scale and scope after 10 years of protein dynamics modelling with Python, Bioinformatics 37 (2021) 3657–3659. https://doi.org/10.1093/bioinformatics/btab187.

[33] T.A. Hall, BioEdit: a user-friendly biological sequence alignment editor and analysis program for Windows 95/98/NT, in: Nucleic Acids Symp. Ser., Oxford, 1999: pp. 95–98. https://www.academia.edu/download/29520866/1999hall1.pdf (accessed July 1, 2025).

[34] W. Humphrey, A. Dalke, K. Schulten, VMD: visual molecular dynamics, J. Mol. Graph. 14 (1996) 33–38, 27–28. https://doi.org/10.1016/0263-7855(96)00018-5.

[35] G. Kemmer, S. Keller, Nonlinear least-squares data fitting in Excel spreadsheets, Nat. Protoc. 5 (2010) 267–281. https://doi.org/10.1038/nprot.2009.182.

[36] Z. Hegedüs, F. Hóbor, D.K. Shoemark, S. Celis, L.-Y. Lian, C.H. Trinh, R.B. Sessions, T.A. Edwards, A.J. Wilson, Identification of β-strand mediated protein–protein interaction inhibitors using ligand-directed fragment ligation, Chem. Sci. 12 (n.d.) 2286–2293. https://doi.org/10.1039/d0sc05694d.

[37] Y. Li, C.H. Trinh, A. Acevedo-Jake, D. Gimenez, S.L. Warriner, A.J. Wilson, Biophysical and structural analyses of the interaction between the SHANK1 PDZ domain and an internal SLiM, Biochem. J. 481 (2024) 945–955. https://doi.org/10.1042/BCJ20240126.

[38] A. Sánta, A. Czajlik, G. Batta, B. Péterfia, Z. Gáspári, Resonance assignment of the Shank1 PDZ domain, Biomol. NMR Assign. 16 (2022) 121–127. https://doi.org/10.1007/s12104-022-10069-4.

[39] H.-J. Lee, J.J. Zheng, PDZ domains and their binding partners: structure, specificity, and modification, Cell Commun. Signal. 8 (2010) 8. https://doi.org/10.1186/1478-811X-8-8.

[40] S. Naisbitt, E. Kim, J.C. Tu, B. Xiao, C. Sala, J. Valtschanoff, R.J. Weinberg, P.F. Worley, M. Sheng, Shank, a Novel Family of Postsynaptic Density Proteins that Binds to the NMDA Receptor/PSD-95/GKAP Complex and Cortactin, Neuron 23 (1999) 569–582. https://doi.org/10.1016/S0896-6273(00)80809-0.

[41] C.H. Jung, S.-H. Ro, J. Cao, N.M. Otto, D.-H. Kim, mTOR regulation of autophagy, FEBS Lett. 584 (2010) 1287–1295. https://doi.org/10.1016/j.febslet.2010.01.017.

[42] K.R. Myers, J.E. Casanova, Regulation of actin cytoskeleton dynamics by Arf-family GTPases, Trends Cell Biol. 18 (2008) 184–192. https://doi.org/10.1016/j.tcb.2008.02.002.

[43] A.Ö. Sungur, K.J. Vörckel, R.K.W. Schwarting, M. Wöhr, Repetitive behaviors in the Shank1 knockout mouse model for autism spectrum disorder: developmental aspects and effects of social context, J. Neurosci. Methods 234 (2014) 92–100. https://doi.org/10.1016/j.jneumeth.2014.05.003.

[44] S. Hagmeyer, A.K. Sauer, A.M. Grabrucker, Prospects of Zinc Supplementation in Autism Spectrum Disorders and Shankopathies Such as Phelan McDermid Syndrome, Front. Synaptic Neurosci. 10 (2018) 11. https://doi.org/10.3389/fnsyn.2018.00011.

[45] M. Miski, Á. Weber, K. Fekete-Molnár, B.M. Keömley-Horváth, A. Csikász-Nagy, Z. Gáspári, Simulated complexes formed from a set of postsynaptic proteins suggest a

localised effect of a hypomorphic Shank mutation, (2023) 2023.10.16.562557. https://doi.org/10.1101/2023.10.16.562557.

1.

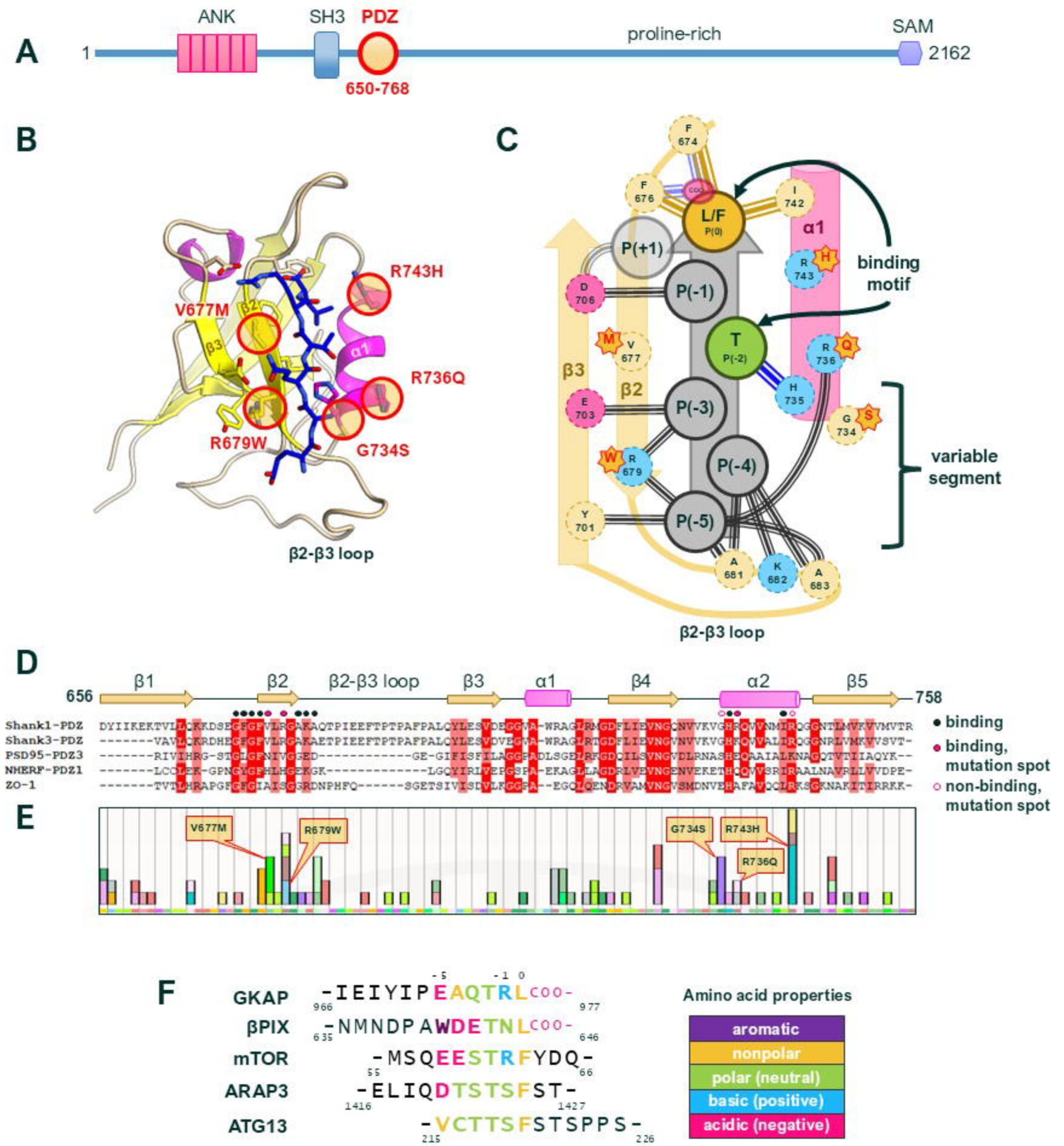
A
ANK
SH3
PDZ
proline-rich
SAM
1
2162
650-768
B
V677M
R743H
R736Q
R679W
G734S
β2-β3 loop
C
L/F
P(0)
P(+1)
P(-1)
T
P(-2)
P(-3)
P(-4)
P(-5)
binding motif
variable segment
β2-β3 loop
D
656
758
β1
β2
β2-β3 loop
β3
α1
β4
α2
β5
Shank1-PDZ
Shank3-PDZ
PSD95-PDZ3
NHERF-PDZ1
ZO-1
binding
binding, mutation spot
non-binding, mutation spot
E
V677M
R679W
G734S
R743H
R736Q
F
GKAP
βPIX
mTOR
ARAP3
ATG13
Amino acid properties
aromatic
nonpolar
polar (neutral)
basic (positive)
acidic (negative)

2.

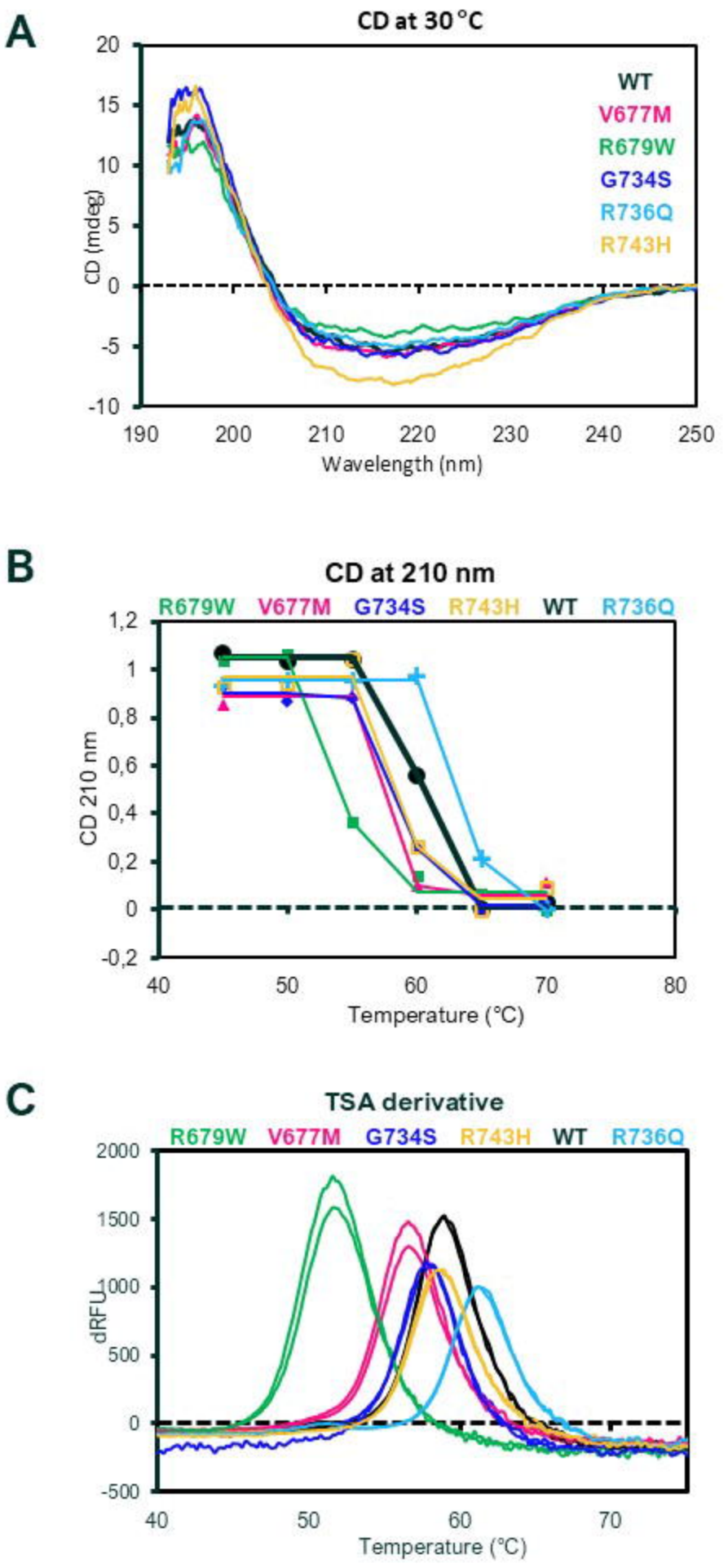
A
CD at 30 °C
WT
V677M
R679W
G734S
R736Q
R743H
CD (mdeg)
Wavelength (nm)
B
CD at 210 nm
R679W V677M G734S R743H WT R736Q
CD 210 nm
Temperature (°C)
C
TSA derivative
R679W V677M G734S R743H WT R736Q
dRFU
Temperature (°C)

3.

A

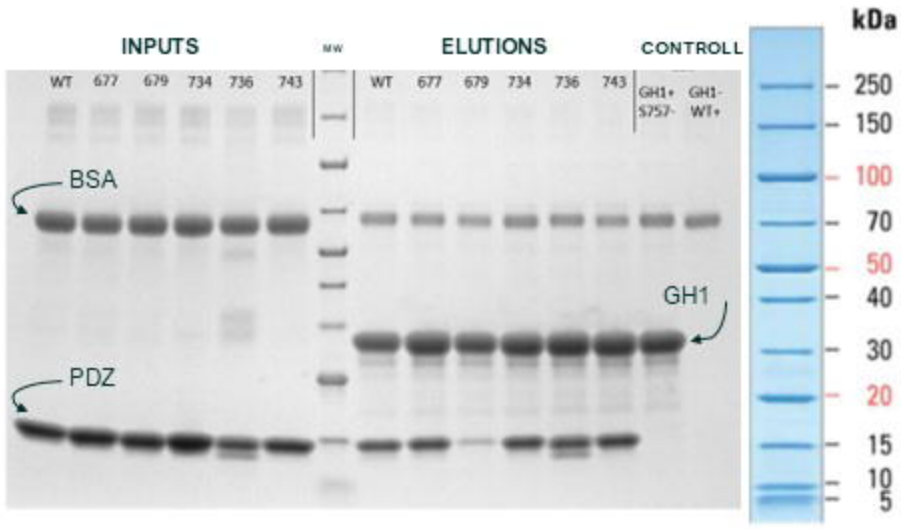
INPUTS
MW
ELUTIONS
CONTROLL
WT 677 679 734 736 743
WT 677 679 734 736 743
GH1+ S757-
GH1- WT+
BSA
PDZ
GH1
kDa
250
150
100
70
50
40
30
20
15
10
5

B

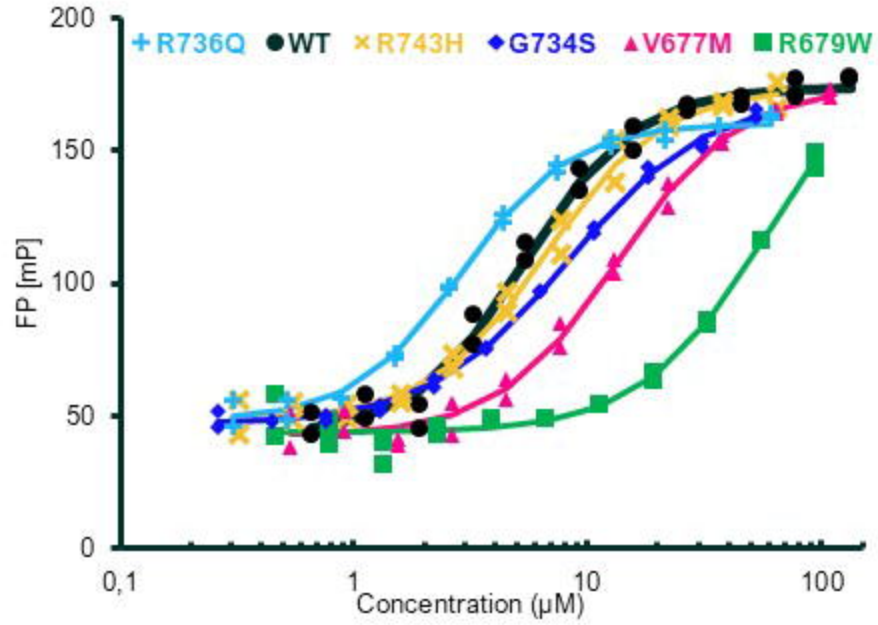
R736Q
WT
R743H
G734S
V677M
R679W
FP [mP]
200
150
100
50
0
0,1
1
10
100
Concentration (µM)

C

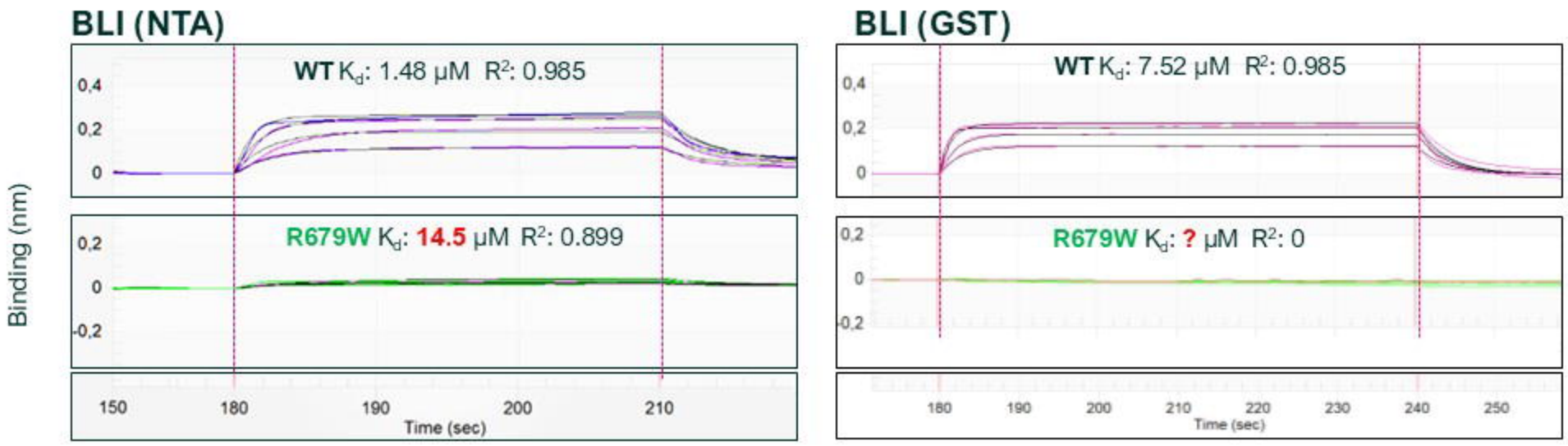
BLI (NTA)
BLI (GST)
Binding (nm)
WT Kd: 1.48 µM R2: 0.985
R679W Kd: 14.5 µM R2: 0.899
WT Kd: 7.52 µM R2: 0.985
R679W Kd: ? µM R2: 0
0,4
0,2
0
-0,2
150
180
190
200
210
220
230
240
250
Time (sec)

4.

A

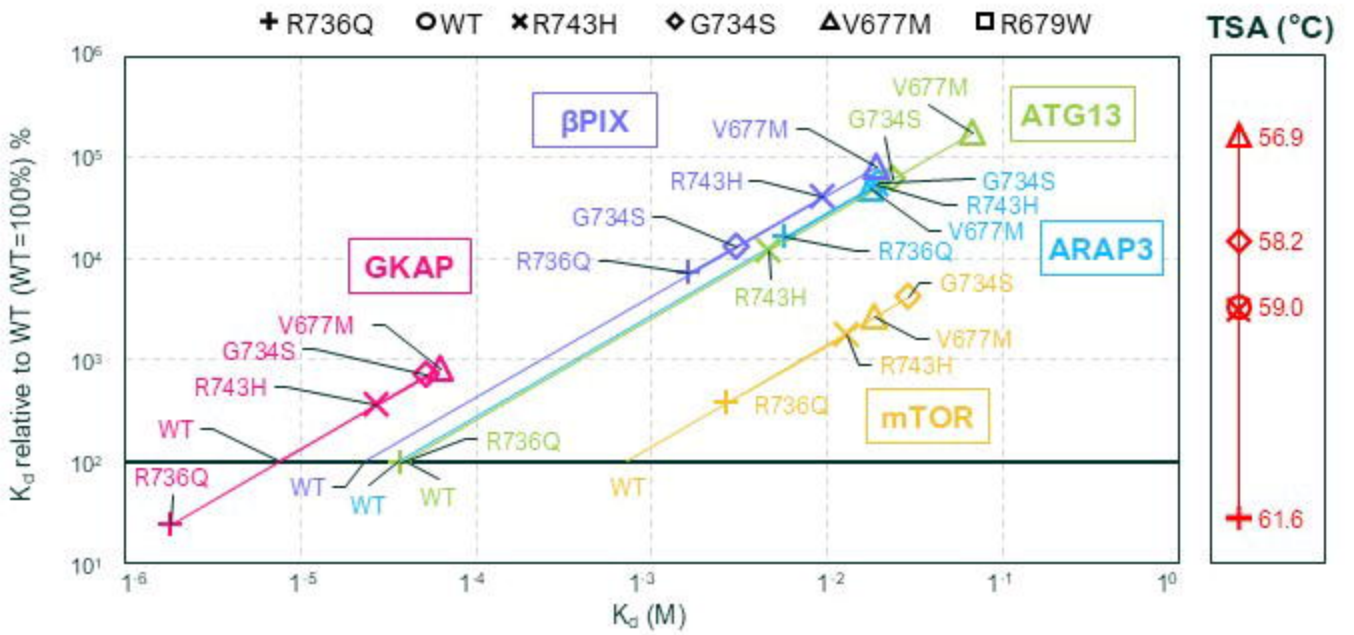

B

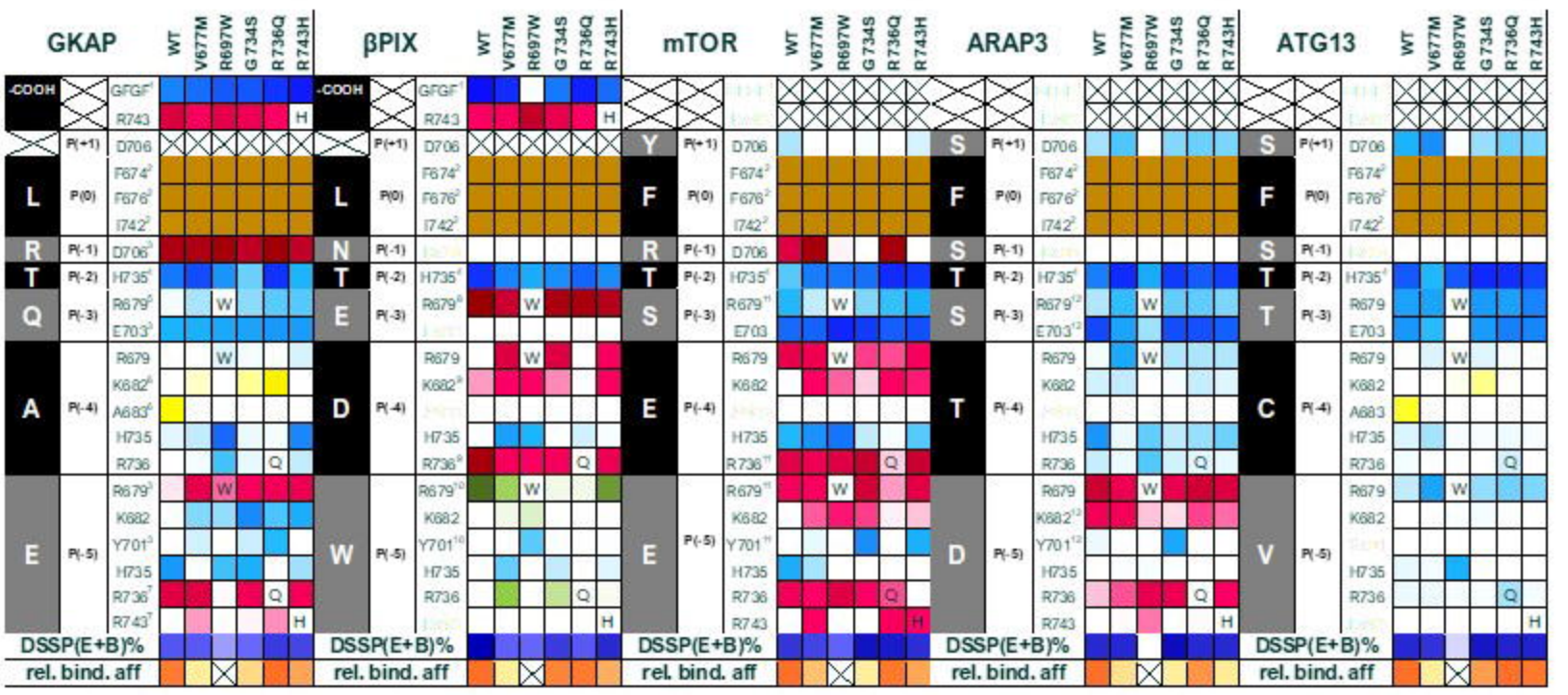

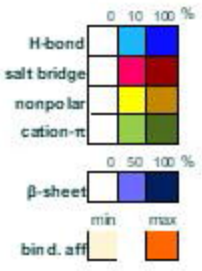

[1]Conserved carboxilate binding motif. [2]
[2]Hydrophobic cavity accomodating C-terminal sidechain. [2–5,7]
[3]Described in GKAP-bound structures. [2,7]
[4]Signature conserved interaction of Shank1's class of PDZ domains. [2]
[5]Described as H-bond in 1Q3P, salt bridge in 5OVC [2,7]
[6]Described in 5OVC [7]
[7]Suggested by analogous interaction theorized by Hegedüs et al. [36]
[8]Described in 3QJN and 3L4F [3,4]
[9]Described as electrostatic in 3L4F [4]
[10]Described as hydrophobic in 3L4F [4]
[11]Analogous interaction in 8S1R [37]
[12]Similar interaction in ARAP3-bound 7A9B [5]

5.

A

	APO	GKAP	βPIX	mTOR	ARAP3	ATG13
WT	40%	15%	18%	20%	5%	26%
V677M	25%	40%	20%	24%	37%	16%
R679W	36%	39%	16%	13%	11%	41%
G734S	25%	44%	15%	21%	9%	40%
R736Q	42%	47%	51%	29%	16%	22%
R743H	42%	31%	10%	19%	21%	26%

Helical (G+H+I+T) DSSP (680-690) (%)

B

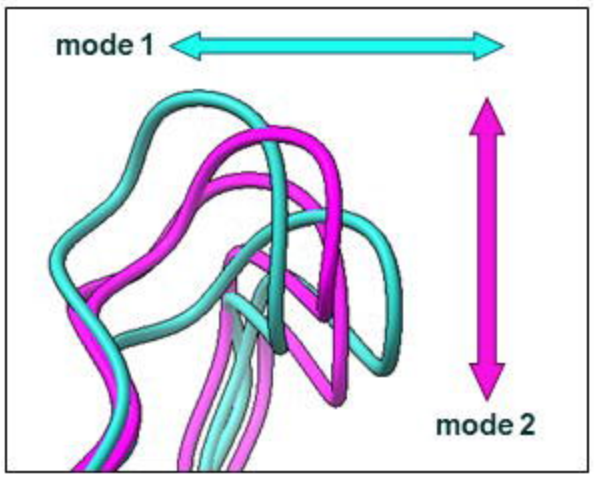

C

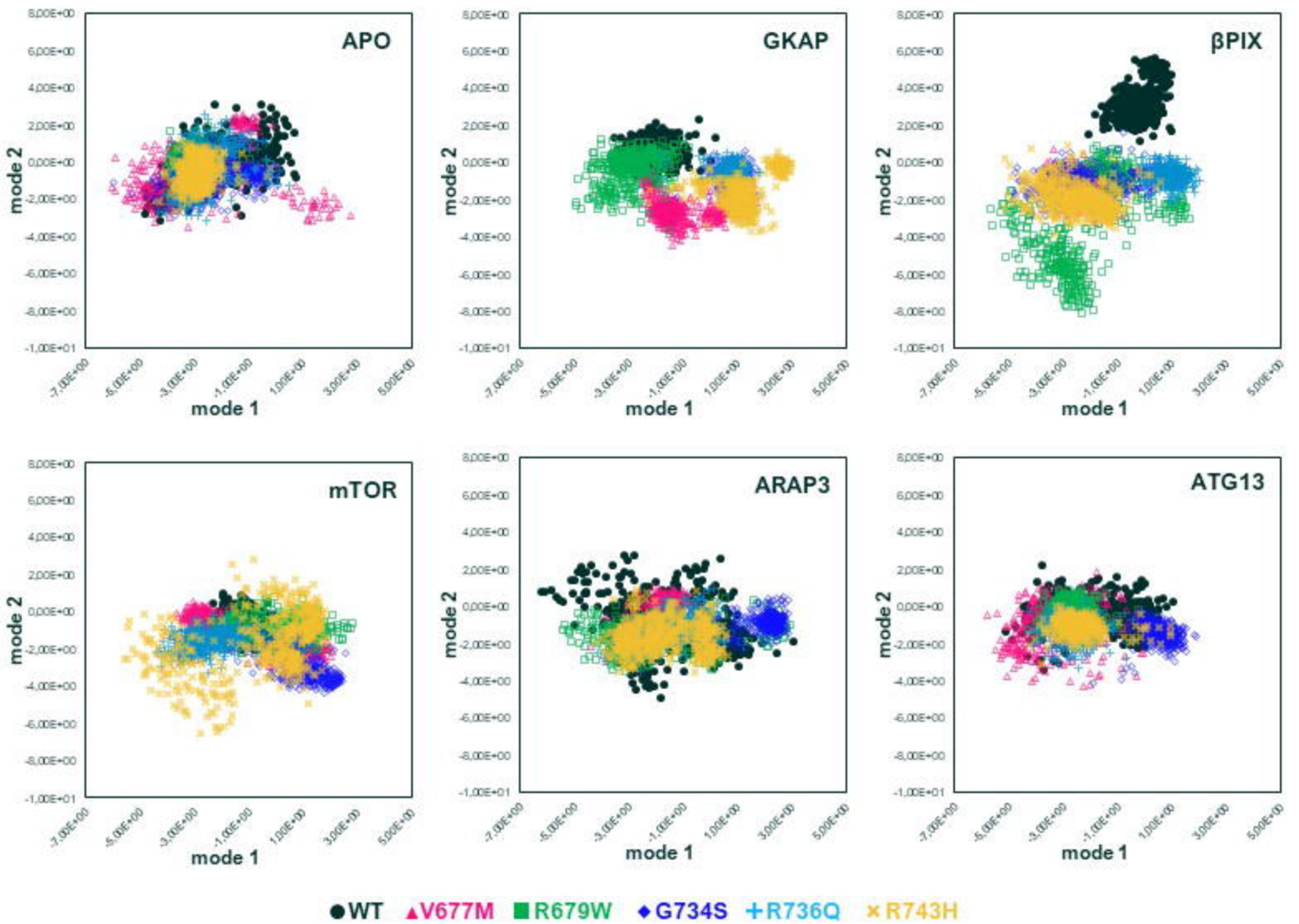

6.

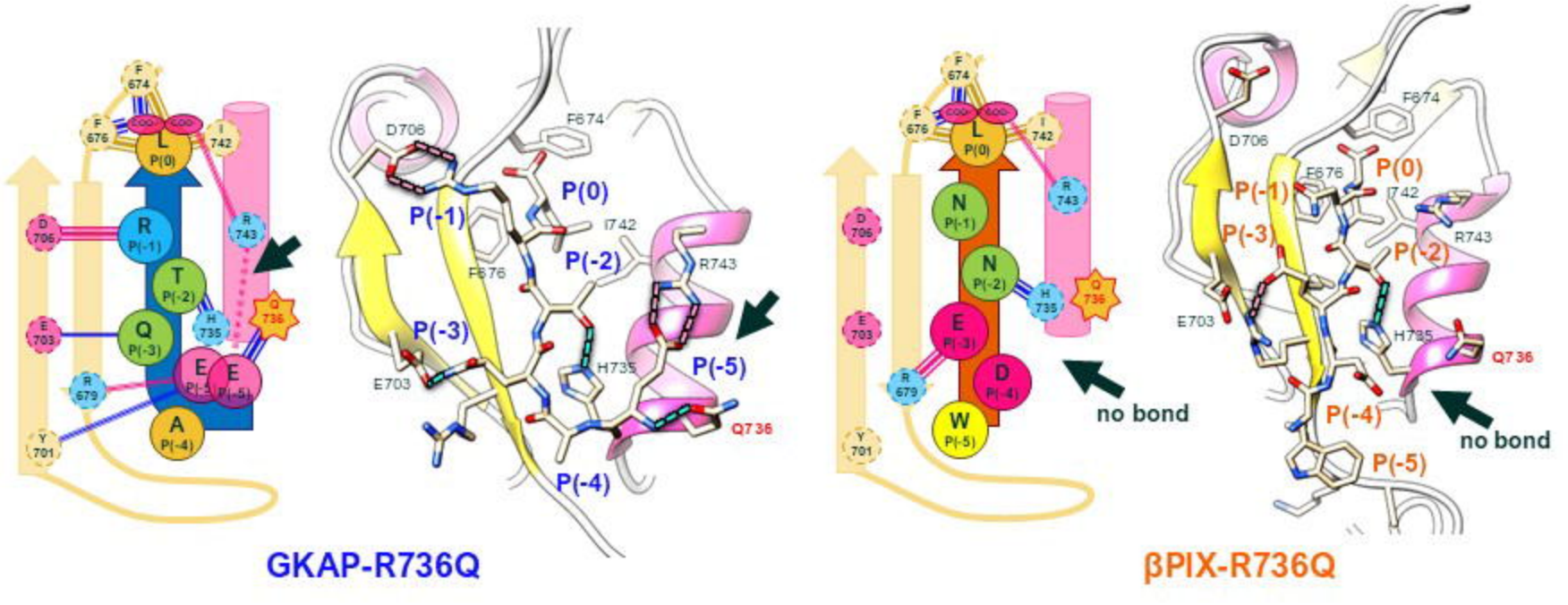

GKAP-R736Q

βPIX-R736Q

7.

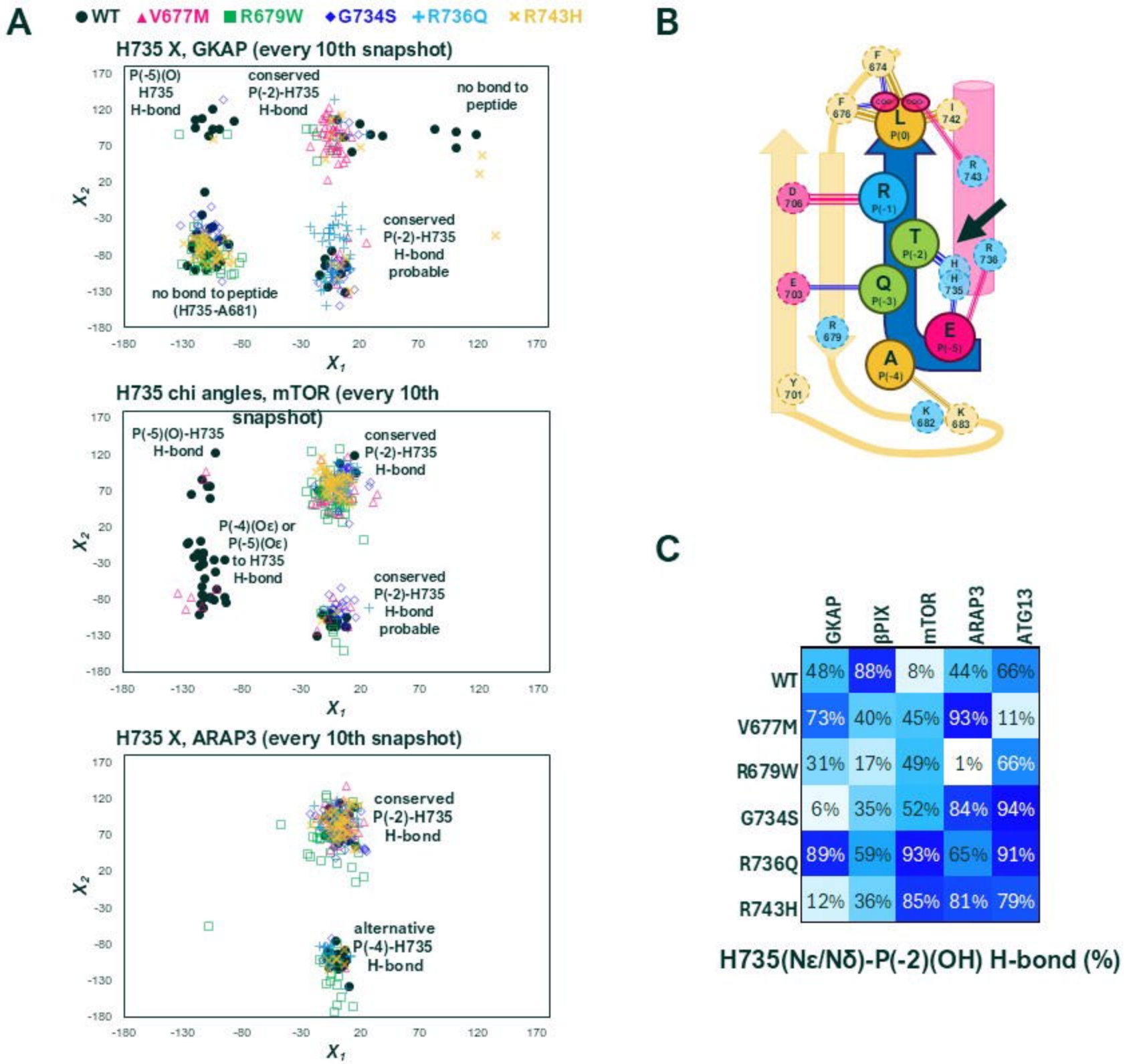
A
WT
V677M
R679W
G734S
R736Q
R743H
H735 X, GKAP (every 10th snapshot)
P(-5)(O) H735 H-bond
conserved P(-2)-H735 H-bond
no bond to peptide
conserved P(-2)-H735 H-bond probable
no bond to peptide (H735-A681)
H735 chi angles, mTOR (every 10th snapshot)
P(-5)(O)-H735 H-bond
conserved P(-2)-H735 H-bond
P(-4)(Oε) or P(-5)(Oε) to H735 H-bond
conserved P(-2)-H735 H-bond probable
H735 X, ARAP3 (every 10th snapshot)
conserved P(-2)-H735 H-bond
alternative P(-4)-H735 H-bond
X1
X2
B
C
GKAP βPIX mTOR ARAP3 ATG13
WT 48% 88% 8% 44% 66%
V677M 73% 40% 45% 93% 11%
R679W 31% 17% 49% 1% 66%
G734S 6% 35% 52% 84% 94%
R736Q 89% 59% 93% 65% 91%
R743H 12% 36% 85% 81% 79%
H735(Nε/Nδ)-P(-2)(OH) H-bond (%)